Computers and Chemical Engineering 192 (2025) 108860

Contents lists available at ScienceDirect

Computers and Chemical Engineering

journal homepage: www.elsevier.com/locate/cace

Solving crystallization/precipitation population balance models in CADET, Part II: Size-based Smoluchowski coagulation and fragmentation equations in batch and continuous modes

Wendi Zhang [a], Todd Przybycien [a], Jan Michael Breuer [b], Eric von Lieres [b,c,*]

[a] Rensselaer Polytechnic Institute, Department of Chemical and Biological Engineering, Troy, 12180, NY, USA
[b] Forschungszentrum Jülich, IBG-1: Biotechnology, Jülich, 52428, Germany
[c] RWTH Aachen University, Computational Systems Biotechnology, Aachen, 52074, Germany

ARTICLE INFO

Keywords:
Smoluchowski coagulation equation
Fragmentation equation
Analytical Jacobians
Open source CADET software
Stirred tank and dispersive plug flow reactors
Finite volume

ABSTRACT

A particle size-based Smoluchowski coagulation and fragmentation equation was solved in the free and open source process modeling package CADET. The WFV and MCNP schemes were selected to discretize the internal particle size coordinate. Weights in these schemes were modified to preserve and conserve the zeroth and third moments for size-based equations. Modified propositions and proofs for the scheme are provided. Analytical Jacobians were derived and implemented to reduce the solver's runtime. A two-dimensional Smoluchowski coagulation and fragmentation equation with axial position as external coordinate was formulated and discretized to support simulations of continuous particulate processes in dispersive plug flow reactors. Five 1D and four 2D test cases were used to validate the implementation and benchmark the solver's performance. The runtime, L1 error norm, L1 error rate, particle size distribution moments up to sixth order and several scalar metrics were analyzed in detail.

1. Introduction

The population balance model (PBM) is in wide use for the modeling of particulate processes including crystallization, precipitation, aerosol formation, granulation, polymerization, agglomeration and fragmentation. The PBM takes into account important crystallization/precipitation mechanisms including nucleation, growth, growth rate dispersion, aggregation and fragmentation processes. In part I we solved the PBM considering nucleation, growth, and growth rate dispersion mechanisms in stirred tank reactors (STRs) and in dispersive plug flow reactors (DPFRs) (Zhang et al., 2024). The model and algorithm were implemented and executed in the free and open-source process modeling software package CADET. In part II, we extend the model and code by incorporating a size-based Smoluchowski coagulation and fragmentation equation to account for particle aggregation and breakage mechanisms.

The discrete Smoluchowski coagulation equation was originally proposed by Smoluchowski (1916) to describe the coagulation of colloids that are subject to Brownian motions using a statistical physics approach. Later, (Müller, 1928) provided a continuous formulation. The coagulation equation tracks the evolution of the particle number distribution due to binary aggregation (coalescence, coagulation, agglomeration) processes in which two smaller particles merge into a larger particle. It presumes that the total volume or mass in the system is conserved while the particle count is reduced during aggregation. The fragmentation equation shares the same mathematical origin with the Smoluchowski coagulation equation but describes the opposed process: it tracks the evolution of the particle distribution when larger particles break into smaller particles. It also presumes that the total volume or mass is conserved, but the particle count increases. Both equations were originally formulated for one-dimensional (1D) processes in well-mixed batch or continuous STRs. They are not directly applicable to the continuous two-dimensional (2D) processes that occur in DPFRs.

Mathematically, the governing equations of the Smoluchowski coagulation and fragmentation model are integro-differential equations. Analytical solutions, when available, are rarely of practical use, as they require special initial conditions. Various authors have developed different numerical methods to solve the governing equations. Well-known solution methods include, but are not limited to, (1) sectional methods such as the fixed pivot method (Kumar and Ramkrishna, 1996) and the cell average technique (Kumar et al., 2006), (2) discretization methods such as the finite volume method (Forestier-Coste and Mancini, 2012; Filbet and Laurençot, 2004; Qamar and Warnecke, 2007; Singh, 2021; Saha et al., 2016; Kumar and Kumar, 2013), finite

* Corresponding author at: Forschungszentrum Jülich, IBG-1: Biotechnology, Jülich, 52428, Germany.
E-mail address: e.von.lieres@fz-juelich.de (E. von Lieres).

https://doi.org/10.1016/j.compchemeng.2024.108860
Received 17 July 2024; Received in revised form 30 August 2024; Accepted 31 August 2024
Available online 6 September 2024

element method (Mahoney and Ramkrishna, 2002) and the discontinuous Galerkin method (Hailiang et al., 2019), and (3) statistical methods such as Monte Carlo simulations (Eibeck and Wagner, 2000, 2001) and methods of moments including direct quadrature methods of moments (Marchisio and Fox, 2005) and extended quadrature methods of moments (Yuan et al., 2012). Among these methods, the finite volume method (FVM) fully recovers the particle size distribution while providing a relatively simple mathematical formulation.

In addition to the full distribution itself, higher order moments of the distribution are of particular interest in many applications since they represent physical quantities, some of which can be directly measured using experiments. Moments also provide distribution-related scalar metrics such as the mean size, total particle count and variance of the particle size distribution. Moment analysis is frequently used to evaluate the efficacy of numerical algorithms because higher order moments are very sensitive to errors in the solution of the governing equations.

Direct application of the FVM for solving the Smoluchowski coagulation and fragmentation equations is difficult, but highly specialized algorithms have been developed. Based on the FVM, (Filbet and Laurençot, 2004) have proposed a numerical scheme for the 1D coagulation equation, which was later extended to higher dimensions by Qamar and Warnecke (2007). Forestier-Coste and Mancini (2012) and Filbet and Laurençot (2004) used cell overlapping to formulate the finite volume preserving scheme that preserves the first order moment or the total volume on nonuniform grids. This approach was later applied to a mass-based Smoluchowski coagulation equation and higher-dimensional cases by Singh (2021). Kaur et al. (2017) formulated a weighted finite volume (WFV) method that preserves the zeroth and first order moments by introducing two weights in the FVM discretized source and sink terms. The scheme was shown to provide shorter runtimes as compared to the FVP scheme for multivariate aggregation problems. To solve the fragmentation equation using the FVM, Bourgade and Filbet (2007) proposed a numerical scheme for binary particle fragmentation with the total volume conserved. To track multiple fragments, Kumar and Kumar (2013) presented another scheme to solve a general fragmentation equation that also conserves the total volume and has second order convergence, independent of the grid type. Later, both schemes were improved by Saha and Bück (2021) resulting in much smaller numerical errors for the total particle count. Saha et al. (2016) introduced the mass conserving and number preserving (MCNP) scheme on nonuniform grids using two weights in the discretized source and sink terms. This scheme preserves the zeroth and first order moments.

In this article, the WFV and MCNP schemes were used due to their moment preservation and conservation properties and thorough documentation. Additionally, no other higher order scheme with similar conservation and preservation properties, yet computationally more efficient, is currently known to us. The WFV and MCNP schemes were originally derived for the particle volume v as the internal coordinate, which is a common model when aggregation and breakage are decoupled from the nucleation and growth mechanisms in the PBM. However, a formulation based on particle size x is more convenient when other mechanisms are also considered in the PBM since the kinetic expressions for nucleation and growth are often based on particle size. However, only a few articles, published in the 1990s, have considered the numerical aspects of the size-based governing equations, e.g. Lister et al. (1995), Hounslow et al. (1988, 2001), Smit et al. (1994), who used a sectional method to solve the equations.

All model equations and numerical algorithms described here were implemented and tested in CADET (von Lieres and Andersson, 2010; Leweke and von Lieres, 2018), a modular, free, and open-source process modeling software package with a C++ core and a Python interface. CADET comprises a variety of unit operations, including reactors, pumps, valves, tubes, tanks, and uses state-of-art numerical algorithms and scientific computing techniques to efficiently assemble and solve the underlying differential–algebraic equations. Arbitrarily many unit operations can be combined, including closed loops and temporal switches, to facilitate integrated process modeling. CADET uses the backward differential formula (BDF) implemented in the implicit differential–algebraic solver (IDAS) as time integrator. Application of the BDF to the size-based FVP and MCNP schemes yields nonlinear algebraic equations that are solved using Newton iteration. Automatic differentiation (AD) was implemented in a previous release to provide the system Jacobian (Püttmann et al., 2016). However, computing and carrying over the Jacobian in computer memory using AD requires computational effort and increases runtime. Hence, analytical Jacobians were derived and implemented to reduce computational burden and enhance solver performance. Optionally, parameter sensitivities can be computed using different AD techniques, which provide valuable information and are required for some optimization algorithms when inverse problems are considered.

The purpose and scope of the work presented here is to: 1. adapt the WFV and MCNP schemes to size-based Smoluchowski coagulation and fragmentation equations and; 2. implement, validate and benchmark the algorithms for the solution of 1D and 2D cases with a particular focus on the 2D cases, in the free and open-source software CADET.

2. Governing equations

2.1. Smoluchowski coagulation equation

The Smoluchowski coagulation equation tracks temporal changes in the particle distribution as a result of particle aggregation/agglomeration processes. It is based on a representative particle property, which can be the particle volume or size. The most common continuous formulation is based on the particle volume v as the internal coordinate (Smoluchowski, 1916):

$$\frac{\partial n_v}{\partial t} = \frac{1}{2}\int_0^v \beta(v-\tilde{v},\tilde{v})n_v(v-\tilde{v})n_v(\tilde{v})\mathrm{d}\tilde{v} - n_v(v)\int_0^\infty \beta(v,\tilde{v})n_v(\tilde{v})\mathrm{d}\tilde{v},$$

in $(0,T_{\mathrm{end}})\times\mathbb{R}^+$, where $\beta:\mathbb{R}^2\to\mathbb{R}$ is the aggregation kernel specific to the aggregation mechanism and $n_v(t,v):(0,T_{\mathrm{end}})\times\mathbb{R}^+\to\mathbb{R}^+$ is the number density based on particle volume. On the right hand side of the equation, the first term is a source term denoting the birth of aggregates of a given volume while the second term is a sink term denoting the disappearance of particles of a given volume by aggregation with others and become larger particles. Mass is conserved in the aggregation process.

To solve the Smoluchowski coagulation equation along with other terms of the PBM including particle nucleation and growth which usually use the particle size $x\in\mathbb{R}^+$ as the internal coordinate, we first convert the above equation to a size-based form. According to Hounslow et al. (2001), Hounslow (1990), the number of particles formed by aggregation in the volume interval $[k_v x^3, k_v x^3 + d(k_v x^3)]$, $d\in\mathbb{R}^+$, is identical to the number of particles formed in the size interval $[x, x+dx]$, described by the differential:

$$n_v \mathrm{d}(k_v x^3) = n\mathrm{d}x, \tag{1}$$

where $n:(0,T_{\mathrm{end}})\times\mathbb{R}^+\to\mathbb{R}^+$ is the number density function based on the particle size, and $k_v\in\mathbb{R}^+$ is the volumetric particle shape factor. Using the above identity, the following particle size-based equation is derived on $(0,T_{\mathrm{end}})\times\mathbb{R}^+$ with details provided in the supplementary material section 1:

$$\begin{aligned}\frac{\partial n(x)}{\partial t} = \frac{x^2}{2}\int_0^x \frac{\beta\left((x^3-\lambda^3)^{\frac{1}{3}},\lambda\right)}{(x^3-\lambda^3)^{\frac{2}{3}}} n\left((x^3-\lambda^3)^{\frac{1}{3}}\right)n(\lambda)\mathrm{d}\lambda \\ - n(x)\int_0^\infty \beta(x,\lambda)n(\lambda)\mathrm{d}\lambda.\end{aligned} \tag{2}$$

We note that the first integral converges with $\lim_{x\to 0} n(x) = 0$. The above equation can be extended to accommodate simulations of stirred tank reactors (STRs) with reactor volume $V : (0, T_{\text{end}}) \to \mathbb{R}^+$

$$\frac{\partial (n(x)V)}{\partial t} = F_{in} n_{in}(x) - F_{out} n(x) + V\left(\frac{x^2}{2} \int_0^x \frac{\beta\left((x^3-\lambda^3)^{\frac{1}{3}}, \lambda\right)}{(x^3-\lambda^3)^{\frac{2}{3}}} n\left((x^3-\lambda^3)^{\frac{1}{3}}\right) n(\lambda)\mathrm{d}\lambda \; - n(x) \int_0^\infty \beta(x,\lambda) n(\lambda)\mathrm{d}\lambda \right), \tag{3}$$

where $F_{in}, F_{out} : (0, T_{\text{end}}) \to \mathbb{R}^+$ are the volumetric inflow and outflow rates and $n_{in} : (0, T_{\text{end}}) \times \mathbb{R}^+ \to \mathbb{R}^+$ is the seed distribution entering the reactor. An additional equation is required to track variations in the reactor's volume in the case of unequal inflow and outflow rates:

$$\frac{\mathrm{d}V}{\mathrm{d}t} = F_{in} - F_{out}. \tag{4}$$

Arbitrary initial conditions for V and n can be applied to Eqs. (2), (3) and (4).

Lastly, the aggregation kernel β is specific to the underlying aggregation mechanism. Two kernels were considered in this study: (1) the constant kernel $\beta \equiv \beta_0 \in \mathbb{R}^+$, and (2) the Golovin kernel $\beta(x_1, x_2) := \beta_0(x_1^3 + x_2^3)$. The first kernel represents the simplest mechanism where all particles undergo an aggregation process at the same constant rate, regardless of their size. The second kernel was named after Golovin after he provided an analytical solution to a cloud droplet growth problem (Golovin, 1963). This kernel describes an aggregation rate which is proportional to the sum of the volumes of the aggregating particles. In addition to the two kernels that are used in this study, we have also implemented other kernels in CADET that are commonly seen in the literature, including the Brownian kernel, Smoluchowski kernel and the differential force kernel.

2.2. Fragmentation equation

Assigning the particle volume as the internal coordinate, the continuous fragmentation equation is (Saito, 1958):

$$\frac{\partial n_v}{\partial t} = \int_v^\infty S(\tilde{v}) b(v|\tilde{v}) n_v(\tilde{v})\mathrm{d}\tilde{v} - S(v) n_v(v),$$

in $(0, T_{\text{end}}] \times \mathbb{R}^+$, where $b : \mathbb{R}^+ \times \mathbb{R}^+ \to \mathbb{R}^+$ is the probability density function for the generation of daughter particles and $S : \mathbb{R}^+ \to \mathbb{R}^+$ is the selection function which determines the rate of fragmentation.

Similar to Eq. (1), the probability density function b can also be converted to its size-based counterpart:

$$b(v|\tilde{v})\mathrm{d}(k_v x^3) = b(x|\lambda)\mathrm{d}x. \tag{5}$$

Using the above equation combined with Eq. (1), the following particle size-based fragmentation equation is derived:

$$\frac{\partial n(x)}{\partial t} = \int_x^\infty S(\lambda) b(x|\lambda) n(\lambda)\mathrm{d}\lambda - S(x) n(x). \tag{6}$$

And as for coagulation, the above fragmentation equation can be extended to accommodate STR operations:

$$\frac{\partial (n(x)V)}{\partial t} = F_{in} n_{in} - F_{out} n + V\left(\int_x^\infty S(\lambda) b(x|\lambda) n(\lambda)\mathrm{d}\lambda - S(x) n(x) \right). \tag{7}$$

In case of variable reactor contents volume, Eq. (7) needs to be solved together with Eq. (4). Arbitrary initial conditions for fIf not otherwise stated,V and n can be used.

The probability density function b for daughter particles must satisfy two requirements:

$$\int_0^\lambda x^3 b(x|\lambda)\mathrm{d}x = \lambda^3, \qquad N(\lambda) = \int_0^\lambda b(x|\lambda)\mathrm{d}x \geq 1, \tag{8}$$

where N is the total number of daughter particles that a mother particle can generate on average, meaning that it can be a non-integer number. The first equation states that the particle of size λ (volume λ^3) is broken up into smaller particles such that the total particle volume is conserved. The second equation states that the average number of daughter particles into which a mother particle breaks cannot be smaller than one.

Lastly, we have implemented the general expressions for both $b(x|\lambda)$ and $S(x)$ proposed by Randolph and Ranjan (1977):

$$S(x) = S_0 x^{3\alpha}, \qquad b(x|\lambda) = 3x^2 \frac{\gamma}{\lambda^3} \left(\frac{x^3}{\lambda^3}\right)^{\gamma-2}, \tag{9}$$

where $S_0 \geq 0$ is the breakage rate constant, $\alpha \in \mathbb{R}^+$ reckons the breakage rate as a function of particle volume and $\gamma > 1$ determines the average number of daughter particles into which a mother particle breaks. The probability density function b satisfies the requirements in Eq. (8) and gives $N(\lambda) = \gamma/(\gamma - 1)$.

2.3. Unified governing equations in STRs and DPFRs

Combining the aggregation and fragmentation balances with our part I work (Zhang et al., 2024), the following governing equation describes simultaneous particle nucleation, growth, growth rate dispersion, aggregation and fragmentation processes in an STR format, in $(0, T_{\text{end}}] \times \mathbb{R}^{\geq x_c}$, with $x_c > 0$ being the minimal particle size considered:

$$\frac{\partial (nV)}{\partial t} = F_{in} n_{in} - F_{out} n - V\left(\frac{\partial (v_G n)}{\partial x} - D_g \frac{\partial^2 n}{\partial x^2} + \frac{x^2}{2} \int_{x_c}^{\hat{x}} \frac{\beta\left((x^3-\lambda^3)^{\frac{1}{3}}, \lambda\right)}{(x^3-\lambda^3)^{\frac{2}{3}}} n\left((x^3-\lambda^3)^{\frac{1}{3}}\right) n(\lambda)\mathrm{d}\lambda \; - n(x) \int_{x_c}^\infty \beta(x,\lambda) n(\lambda)\mathrm{d}\lambda + \int_x^\infty S(\lambda) b(x|\lambda) n(\lambda)\mathrm{d}\lambda - S(x) n(x) \right). \tag{10}$$

Note that the upper integral boundary of the aggregation term $\hat{x} := (x^3 - x_c^3)^{\frac{1}{3}}$ is required to enforce the minimum considered particle size, which was introduced to model nucleation with a critical nuclei size x_c via the boundary condition. The nucleation and regularity boundary conditions are given in $(0, T_{\text{end}}]$

$$\left(n v_G - D_g \frac{\partial n}{\partial x}\right)\Big|_{x=x_c} = B_0, \qquad \left(n v_G - D_g \frac{\partial n}{\partial x}\right)\Big|_{x\to\infty} = 0, \tag{11}$$

where $B_0 \geq 0$ is the nucleation kinetics. To account for the spatial variations in a DPFR format, we consider axial convection and diffusion with axial position $z \in [0, L]$ as the external coordinate, giving us the combined governing equation in $(0, T_{\text{end}}] \times (0, L] \times \mathbb{R}^+$

$$\frac{\partial n(x,z)}{\partial t} = -v_{ax} \frac{\partial n(x,z)}{\partial z} + D_{ax} \frac{\partial^2 n(x,z)}{\partial z^2} - \frac{\partial (v_G(x) n(x,z))}{\partial x} + D_g \frac{\partial^2 n(x,z)}{\partial x^2} + B_0 \delta(x - x_c) + \frac{x^2}{2} \int_{x_c}^{\hat{x}} \frac{\beta\left((x^3-\lambda^3)^{\frac{1}{3}}, \lambda, z\right)}{(x^3-\lambda^3)^{\frac{2}{3}}} n\left((x^3-\lambda^3)^{\frac{1}{3}}, z\right) n(\lambda, z)\mathrm{d}\lambda - n(x,z) \int_{x_c}^\infty \beta(x,\lambda,z) n(\lambda,z)\mathrm{d}\lambda + \int_x^\infty S(\lambda,z) b(x|\lambda,z) n(\lambda,z)\mathrm{d}\lambda - S(x,z) n(x,z), \tag{12}$$

where $L \geq 0$ is the column length, v_{ax} denotes the axial velocity, and D_{ax} is the axial dispersion coefficient. This form of the population balance equation is complemented by the same nucleation and regularity boundary conditions for the internal coordinate as given in (11). For the external axial direction coordinate, Danckwerts boundary conditions are used in $(0, T_{\text{end}}]$:

$$\left(n v_{ax} - D_{ax} \frac{\partial n}{\partial z}\right)\Big|_{z=0} = v_{ax} n_{in,x}, \qquad \frac{\partial n}{\partial z}\Big|_{z=L} = 0. \tag{13}$$

A mass balance equation can be solved along with either of the STR or DPFR population balance equations to describe the residual solution concentration of the precipitating or crystallizing solute. Since mass is conserved by the aggregation and fragmentation processes, the corresponding mass balance equations are the same as Eq. 8 and Eq. 15 in Zhang et al. (2024) and are omitted here.

3. Finite volume discretization

To apply the finite volume method, we first discretize the internal coordinate x on the particle size domain, obtaining the cell boundaries $x_c = x_{\frac{1}{2}} < x_{\frac{3}{2}} < \ldots < x_{i-\frac{1}{2}} < x_{i+\frac{1}{2}}$. Accordingly, the size of a cell with index i is $\Delta x_i = x_{i+\frac{1}{2}} - x_{i-\frac{1}{2}}$ and the cell center is $x_i = (x_{i+\frac{1}{2}} + x_{i-\frac{1}{2}})/2$. The cell average number density n_i is given by: $n_i = \frac{1}{\Delta x_i}\int_{x_{i-\frac{1}{2}}}^{x_{i+\frac{1}{2}}} n\mathrm{d}x$. In this article, we make the assumption that the number density is concentrated at the cell centers.

Although the continuous Smoluchowski coagulation equation (2) is mass conserving, its discretized form by the direct application of the FVM is no longer mass conserving. To illustrate the problem, consider a grid with cell average volumes 1, 4, 9, 16, 25, and 36. Aggregation of particles with volumes 4 and 16 would result in particles with volume 20, which is not represented by the grid. Both the WFV and MCNP schemes handle this problem by introducing weights and force the discretized governing equations to obey mass conservation and number preservation. However, these schemes were originally developed for governing equations with the particle volume as internal coordinate. Hence, we adapt the WFV and MCNP schemes for the Smoluchowski coagulation equation (2) and for the fragmentation equation (6), both with particle size as internal coordinate, and we prove that our adaptations also obey mass conservation and number preservation. To facilitate these proofs, we introduce the discrete and continuous jth order moment of the number density distribution n as:

$$M_j^{\Delta} = \sum_{i=1}^{\infty} n_i x_i^j \Delta x_i, \qquad M_j = \int_0^{\infty} n x^j \mathrm{d}x, \tag{14}$$

respectively.

Definition 1. A numerical scheme is third order moment conserving or total volume conserving if

$$\frac{\mathrm{d}M_3}{\mathrm{d}t} = 0, \tag{15}$$

i.e. the third order moment or total volume does not change over time.

The total count of particles varies as a function of time, but can be tracked analytically. For aggregation, integrate equation (2) over the entire domain giving the total number of particles or zeroth moment:

$$\begin{aligned}\frac{\mathrm{d}M_0}{\mathrm{d}t} &= \int_0^{\infty}\frac{x^2}{2}\int_0^{x}\frac{\beta\left((x^3-\lambda^3)^{\frac{1}{3}},\lambda\right)}{(x^3-\lambda^3)^{\frac{2}{3}}} n\left((x^3-\lambda^3)^{\frac{1}{3}}\right) n(\lambda)\mathrm{d}\lambda\mathrm{d}x \\ &\quad - \int_0^{\infty}\int_0^{\infty}\beta(x,\lambda)n(\lambda)n(x)\mathrm{d}\lambda\mathrm{d}x,\end{aligned}$$

change the order of integration in the first term on the right hand side,

$$\begin{aligned}\frac{\mathrm{d}M_0}{\mathrm{d}t} &= \int_0^{\infty}\int_{\lambda}^{\infty}\frac{x^2}{2}\frac{\beta\left((x^3-\lambda^3)^{\frac{1}{3}},\lambda\right)}{(x^3-\lambda^3)^{\frac{2}{3}}} n\left((x^3-\lambda^3)^{\frac{1}{3}}\right) n(\lambda)\mathrm{d}x\mathrm{d}\lambda \\ &\quad - \int_0^{\infty}\int_0^{\infty}\beta(x,\lambda)n(\lambda)n(x)\mathrm{d}\lambda\mathrm{d}x,\end{aligned}$$

define $\tilde{\lambda} = (x^3-\lambda^3)^{\frac{1}{3}}$, accordingly for fixed λ in the inner integral,

$$\mathrm{d}\tilde{\lambda} = \frac{x^2}{(x^3-\lambda^3)^{\frac{2}{3}}}\mathrm{d}x,$$

change of variables,

$$\frac{\mathrm{d}M_0}{\mathrm{d}t} = \frac{1}{2}\int_0^{\infty}\int_0^{\infty}\beta(\tilde{\lambda},\lambda)n(\tilde{\lambda})n(\lambda)\mathrm{d}\tilde{\lambda}\mathrm{d}\lambda - \int_0^{\infty}\int_0^{\infty}\beta(x,\lambda)n(\lambda)n(x)\mathrm{d}\lambda\mathrm{d}x,$$

substituting x by $\tilde{\lambda}$, the above equation simplifies to

$$\frac{\mathrm{d}M_0}{\mathrm{d}t} = -\frac{1}{2}\int_0^{\infty}\int_0^{\infty}\beta(\tilde{\lambda},\lambda)n(\tilde{\lambda})n(\lambda)\mathrm{d}\tilde{\lambda}\mathrm{d}\lambda,$$

invoking the assumption that the mass is concentrated at the cell centers and approximating the integral using the midpoint quadrature rule, the discrete zeroth order moment is:

$$\frac{\mathrm{d}M_0^{\Delta}}{\mathrm{d}t} = -\frac{1}{2}\sum_{i=1}^{\infty}\sum_{j=1}^{\infty}\beta(x_i,x_j)n_i n_j \Delta x_i \Delta x_j. \tag{16}$$

Therefore,

Definition 2. A numerical scheme for the Smoluchowski coagulation equation is zeroth order moment preserving or number preserving if it satisfies Eq. (16).

For fragmentation, integrate equation (6) over the entire domain:

$$\begin{aligned}\frac{\mathrm{d}M_0}{\mathrm{d}t} &= \int_0^{\infty}\left(\int_x^{\infty} S(\lambda)b(x|\lambda)n(\lambda)\mathrm{d}\lambda - S(x)n(x)\right)\mathrm{d}x \\ &= \int_0^{\infty}\int_x^{\infty} S(\lambda)b(x|\lambda)n(\lambda)\mathrm{d}\lambda\mathrm{d}x - \int_0^{\infty} S(x)n(x)\mathrm{d}x,\end{aligned}$$

change the order of integration in the first term on the right hand side

$$\frac{\mathrm{d}M_0}{\mathrm{d}t} = \int_0^{\infty}\int_0^{\lambda} S(\lambda)b(x|\lambda)n(\lambda)\mathrm{d}x\mathrm{d}\lambda - \int_0^{\infty} S(x)n(x)\mathrm{d}x,$$

insert the definition of $N(\lambda)$

$$\frac{\mathrm{d}M_0}{\mathrm{d}t} = \int_0^{\infty} S(\lambda)n(\lambda)N(\lambda)\mathrm{d}\lambda - \int_0^{\infty} S(x)n(x)\mathrm{d}x,$$

substituting λ by x the two terms on the right hand side can be combined to

$$\frac{\mathrm{d}M_0}{\mathrm{d}t} = \int_0^{\infty}(N(x)-1)S(x)n(x)\mathrm{d}x.$$

Invoking the assumption that the mass is concentrated at the cell centers and approximating the integral using the midpoint quadrature rule, the discrete zeroth order moment is:

$$\frac{\mathrm{d}M_0^{\Delta}}{\mathrm{d}t} = \sum_{i=1}^{\infty}(N_i-1)S_i n_i \Delta x_i, \tag{17}$$

where $N_i = N(x_i)$ and $S_i = S(x_i)$. Therefore,

Definition 3. A numerical scheme for the fragmentation equation is zeroth order moment preserving or number preserving if it satisfies Eq. (17).

3.1. The weighted finite volume scheme

In the context of aggregation, we refer to the initially smaller particles as mother particles and to the resulting larger particles as daughter particles and define the index set

$$A^l := \left\{(j,k)\in\mathbb{N}^2 : x_{l-\frac{1}{2}} \le (x_j^3 + x_k^3)^{\frac{1}{3}} < x_{l+\frac{1}{2}}\right\}, \tag{18}$$

such that it contains the index combinations of all possible mother particles for a given daughter particle with index l. That is, the total volume of the mother particles is within the cell boundaries of the specified daughter particle index.

We utilize the WFV approach by Kaur et al. (2017) to discretize equation (2). The WFV ensures conservation of total mass and preservation of the total number of particles through its assigned weights, which are based on additive properties like volume or mass. Hence, we modify the weights to account for the volume x^3, rather than the

internal size coordinate x, resulting in the following size-based WFV formulation:

$$\frac{\partial n_i}{\partial t} = \sum_{\substack{(j,k)\in A^i \\ k\geq j}} \left(1-\frac{1}{2}\delta_{j,k}\right)\beta_{jk}n_j n_k \frac{\Delta x_j \Delta x_k}{\Delta x_i}\frac{x_j^3+x_k^3}{2x_i^3-x_j^3-x_k^3} - \sum_{j=1}^{\infty}\beta_{ij}n_i n_j \Delta x_j \frac{x_{l_{ij}}^3}{2x_{l_{ij}}^3-x_i^3-x_j^3}, \tag{19}$$

where $\beta_{jk} = \beta(x_j, x_k)$, $\delta_{j,k}$ is the Kronecker delta and l_{ij} is the index such that $(i,j)\in A^{l_{ij}}$. The above scheme can be used on arbitrary grids.

Proposition 1. *The proposed scheme (19) for the Smoluchowski coagulation equation is total volume conserving.*

Proof. We start with Eq. (19). Since j and k are symmetric, eliminate the constraint $k \geq j$ along with the Kronecker delta, leading to the prefactor 1/2. We then compute the discrete third order moment M_3^Δ according to Eq. (14) by multiplying with x_i^3 and Δx_i and forming the sum over all cells:

$$\frac{\mathrm{d}M_3^\Delta}{\mathrm{d}t} = \frac{1}{2}\sum_{i=1}^{\infty}\sum_{(j,k)\in A^i}\beta_{jk}n_j n_k x_i^3 \Delta x_j \Delta x_k \frac{x_j^3+x_k^3}{2x_i^3-x_j^3-x_k^3} - \sum_{i=1}^{\infty}\sum_{j=1}^{\infty}\beta_{ij}n_i n_j x_i^3 \Delta x_j \Delta x_i \frac{x_{l_{ij}}^3}{2x_{l_{ij}}^3-x_i^3-x_j^3}.$$

The sum over $\sum_{i=1}^{\infty}\sum_{(j,k)\in A^i}$ can be rewritten as the sum over all combinations of j,k

$$\frac{\mathrm{d}M_3^\Delta}{\mathrm{d}t} = \frac{1}{2}\sum_{j=1}^{\infty}\sum_{k=1}^{\infty}\beta_{jk}n_j n_k x_{l_{jk}}^3 \Delta x_j \Delta x_k \frac{x_j^3+x_k^3}{2x_{l_{jk}}^3-x_j^3-x_k^3} - \sum_{i=1}^{\infty}\sum_{j=1}^{\infty}\beta_{ij}n_i n_j x_i^3 \Delta x_j \Delta x_i \frac{x_{l_{ij}}^3}{2x_{l_{ij}}^3-x_i^3-x_j^3},$$

where l_{jk} is defined similarly to l_{ij}. Since j and k are symmetric, we obtain conservation of volume

$$\frac{\mathrm{d}M_3^\Delta}{\mathrm{d}t} = 0. \quad \square$$

Proposition 2. *The proposed scheme (19) for the Smoluchowski coagulation equation is number preserving.*

Proof. We start with Eq. (19) and eliminate the constraint $k \geq j$ along with the Kronecker delta and produce the discrete zeroth order moment M_0^Δ according to Eq. (14) by multiplying with Δx_i and forming the sum over all cells

$$\frac{\mathrm{d}M_0^\Delta}{\mathrm{d}t} = \frac{1}{2}\sum_{i}^{\infty}\sum_{(j,k)\in A^i}\beta_{jk}n_j n_k \Delta x_j \Delta x_k \frac{x_j^3+x_k^3}{2x_i^3-x_j^3-x_k^3} - \sum_{i}^{\infty}\sum_{j}^{\infty}\beta_{ij}n_i n_j \Delta x_j \Delta x_i \frac{x_{l_{ij}}^3}{2x_{l_{ij}}^3-x_i^3-x_j^3}.$$

Reformulating the sum as in the proof for Proposition 1, we obtain

$$\frac{\mathrm{d}M_0^\Delta}{\mathrm{d}t} = \frac{1}{2}\sum_{j}^{\infty}\sum_{k}^{\infty}\beta_{jk}n_j n_k \Delta x_j \Delta x_k \frac{x_j^3+x_k^3}{2x_i^3-x_j^3-x_k^3} - \sum_{i}^{\infty}\sum_{j}^{\infty}\beta_{ij}n_i n_j \Delta x_j \Delta x_i \frac{x_{l_{ij}}^3}{2x_{l_{ij}}^3-x_i^3-x_j^3},$$

and the sum collapses to

$$\frac{\mathrm{d}M_0^\Delta}{\mathrm{d}t} = \sum_{j}^{\infty}\sum_{k}^{\infty}\beta_{jk}n_j n_k \Delta x_j \Delta x_k \left(\frac{1}{2}\frac{x_j^3+x_k^3}{2x_i^3-x_j^3-x_k^3} - \frac{x_i^3}{2x_i^3-x_j^3-x_k^3}\right) = -\frac{1}{2}\sum_{j}^{\infty}\sum_{k}^{\infty}\beta_{jk}n_j n_k \Delta x_j \Delta x_k.$$

According to Definition 2, the total number or the discrete zeroth order moment is preserved. $\square$

3.2. The mass conserving and number preserving scheme

In this section we modify the MCNP scheme introduced by Saha et al. (2016) to discretize equation (6). To this end, we again substitute terms of the volume x^3 instead of the internal coordinate x, and produce the following size-based formulation:

$$\frac{\partial n_i}{\partial t} = \sum_{j=i}^{\infty} S_j n_j Y_j^b \frac{\Delta x_j}{\Delta x_i}\int_{x_{i-\frac{1}{2}}}^{p_i^j} b(x|x_j)\mathrm{d}x - S_i n_i Y_i^d. \tag{20}$$

The modification factors Y_i^b and Y_i^d are given by

$$Y_i^b = \frac{x_i^3(N_i-1)}{\sum_{j=1}^{i}(x_i^3-x_j^3)\int_{x_{j-\frac{1}{2}}}^{x_{j+\frac{1}{2}}} b(x|x_i)\mathrm{d}x}, \qquad Y_i^d = \frac{Y_i^b}{x_i^3}\sum_{j=1}^{i} x_j^3 \int_{x_{j-\frac{1}{2}}}^{p_j^i} b(x|x_i)\mathrm{d}x, \tag{21}$$

where

$$p_i^j = \begin{cases} x_{i+\frac{1}{2}}, & j=i; \\ x_i, & j\neq i. \end{cases} \tag{22}$$

Specifically, $Y_1^b = x_1^3(N_1-1)$ when $i=1$. The proposed scheme can be used on arbitrary grids. Next, we shall prove that the proposed scheme is total volume conserving and number preserving.

Proposition 3. *The proposed scheme (20) for the fragmentation equation is total volume conserving.*

Proof. We begin with Eq. (20) and compute the total volume according to Eq. (14) by multiplying by $x_i^3\Delta x_i$ and forming the sum over all cells

$$\frac{\mathrm{d}M_3^\Delta}{\mathrm{d}t} = \sum_{i}^{\infty}\sum_{j=i}^{\infty} S_j n_j Y_j^b x_i^3 \Delta x_j \int_{x_{i-\frac{1}{2}}}^{p_i^j} b(x|x_j)\mathrm{d}x - \sum_{i}^{\infty} S_i n_i x_i^3 \Delta x_i Y_i^d.$$

We change the order of summation for the first term on the right hand side and insert the definition of Y_i^d and obtain

$$\frac{\mathrm{d}M_3^\Delta}{\mathrm{d}t} = \sum_{j=1}^{\infty} S_j n_j \Delta x_j Y_j^b \sum_{i=1}^{j} x_i^3 \int_{x_{i-\frac{1}{2}}}^{p_i^j} b(x|x_j)\mathrm{d}x - \sum_{j=1}^{\infty} S_j n_j \Delta x_j Y_j^b \sum_{i=1}^{j} x_i^3 \int_{x_{i-\frac{1}{2}}}^{p_i^j} b(x|x_j)\mathrm{d}x = 0,$$

which satisfies Definition 1, indicating that the total volume is conserved for the proposed scheme. $\square$

Proposition 4. *The proposed scheme (20) for the fragmentation equation is number preserving.*

Proof. We begin with Eq. (20) and compute the first order moment by multiplying with Δx_i, and forming the sum over all discrete points

$$\frac{\mathrm{d}M_0^\Delta}{\mathrm{d}t} = \sum_{i=1}^{\infty}\sum_{j=i}^{\infty} S_j n_j Y_j^b \Delta x_j \int_{x_{i-\frac{1}{2}}}^{p_i^j} b(x|x_j)\mathrm{d}x - \sum_{i=1}^{\infty} S_i n_i \Delta x_i Y_i^d.$$

We change the order of summation for the first term, insert the definition of Y_j^d and simplify the equation to obtain

$$\frac{\mathrm{d}M_0^{\Delta}}{\mathrm{d}t} = \sum_{j=1}^{\infty} S_j n_j \Delta x_j Y_j^b \left(\sum_{i=1}^{j} \int_{x_{i-\frac{1}{2}}}^{p_i^j} b(x|x_j)\mathrm{d}x - \frac{1}{x_j^3} \sum_{i=1}^{j} x_i^3 \int_{x_{i-\frac{1}{2}}}^{p_i^j} b(x|x_j)\mathrm{d}x \right)$$
$$= \sum_{j=1}^{\infty} S_j n_j \Delta x_j Y_j^b \frac{1}{x_j^3} \left(\sum_{i=1}^{j} (x_j^3 - x_i^3) \int_{x_{i-\frac{1}{2}}}^{p_i^j} b(x|x_j)\mathrm{d}x \right).$$

We substitute the definition of Y_j^b and obtain

$$\frac{\mathrm{d}M_0^{\Delta}}{\mathrm{d}t} =$$
$$\sum_{j=1}^{\infty} S_j n_j \Delta x_j \frac{x_j^3 (N_j - 1)}{\sum_{j=1}^{i} (x_i^3 - x_j^3) \int_{x_{j-\frac{1}{2}}}^{x_{j+\frac{1}{2}}} b(x|x_i)\mathrm{d}x} \frac{1}{x_j^3} \left(\sum_{i=1}^{j} (x_j^3 - x_i^3) \int_{x_{i-\frac{1}{2}}}^{x_{i+\frac{1}{2}}} b(x|x_j)\mathrm{d}x \right)$$
$$= \sum_{j=1}^{\infty} (N_j - 1) S_j n_j \Delta x_j,$$

This satisfies Definition 3, indicating that the total particle number of the proposed scheme is preserved. □

3.3. Discretization of the 1D governing equations for batch processes

The WFV and MCNP schemes can be directly applied to discretize the source and sink terms of the aggregation and fragmentation parts of Eq. (10), respectively, leaving the axial convection and diffusion terms un-discretized. We refer to Zhang et al. (2024) for details on their FVM discretizations. For the sake of conciseness, we report the final results as:

$$\begin{aligned} n_i \frac{\partial V}{\partial t} + V \frac{\partial n_i}{\partial t} &= F_{in} n_{in,i} - F_{out} n_i \\ &+ \left(-\frac{F_{i+1/2} - F_{i-1/2}}{\Delta x_i} + \frac{\Lambda_{i+1/2} - \Lambda_{i-1/2}}{\Delta x_i} \right. \\ &+ \sum_{\substack{(j,k)\in A^i \\ k\geq j}} \left(1 - \frac{1}{2}\delta_{j,k}\right) \beta_{jk} n_j n_k \frac{\Delta x_j \Delta x_k}{\Delta x_i} \frac{x_j^3 + x_k^3}{2x_i^3 - x_j^3 - x_k^3} \\ &- \sum_{j=1}^{N_x} \beta_{ij} n_i n_j \Delta x_j \frac{x_{l_{ij}}^3}{2x_{l_{ij}}^3 - x_i^3 - x_j^3} \\ &+ \left. \sum_{j=i}^{N_x} S_j n_j Y_j^b \frac{\Delta x_j}{\Delta x_i} \int_{x_{i-\frac{1}{2}}}^{p_i^j} b(x|x_j)\mathrm{d}x - S_i n_i Y_i^d \right) V, \end{aligned} \tag{23}$$

where $n_{in,i} = \frac{1}{\Delta x_i} \int_{x_{i-\frac{1}{2}}}^{x_{i+\frac{1}{2}}} n_{in}\mathrm{d}x$. $F_{i\pm1/2}$ and $\Lambda_{i\pm1/2}$ are the convective and diffusional numerical fluxes at the i^{th} left and right cell faces, respectively. The nucleation source term is enforced as a boundary condition. Note that the upper bound of x is truncated from infinity to a sufficiently large number and that N_x is the total number of cells. As an upper limit of infinity is assumed in the propositions and proofs in the above section, we remark that they are strictly true only when the right boundary of x ($x_{\max} \in \mathbb{R}$) is chosen to be large enough such that truncation of the series does not change the sum.

The diffusional numerical flux was reconstructed using a second-order approximation for a uniform grid which becomes first-order for a nonuniform grid. Although the convective numerical flux was reconstructed using four different schemes, we chose only the HR Koren scheme and the WENO35 scheme for further analysis in this study as they were found to be the most computationally efficient schemes in our previous test cases. The exact expressions for these schemes, along with rigorous benchmarks and discussions of their advantages and disadvantages, can be found in Zhang et al. (2024).

3.4. Discretization of the 2D governing equations for continuous processes

FVM discretizations of Eq. (12) can be done similarly to give:

$$\begin{aligned} \frac{\partial n_{i,p}}{\partial t} &= -\frac{F_{i,p+1/2} - F_{i,p-1/2}}{\Delta z_p} + \frac{\Lambda_{i,p+1/2} - \Lambda_{i,p-1/2}}{\Delta z_p} \\ &- \frac{F_{i+1/2,p} - F_{i-1/2,p}}{\Delta x_i} + \frac{\Lambda_{i+1/2,p} - \Lambda_{i-1/2,p}}{\Delta x_i} \\ &+ \sum_{\substack{(j,k)\in A^i \\ k\geq j}} \left(1 - \frac{1}{2}\delta_{j,k}\right) \beta_{jk,p} n_{j,p} n_{k,p} \frac{\Delta x_j \Delta x_k}{\Delta x_i} \frac{x_j^3 + x_k^3}{2x_i^3 - x_j^3 - x_k^3} \\ &- \sum_{j=1}^{N_x} \beta_{ij,p} n_{i,p} n_{j,p} \Delta x_j \frac{x_{l_{ij}}^3}{2x_{l_{ij}}^3 - x_i^3 - x_j^3} \\ &+ \sum_{j=i}^{N_x} S_{j,p} n_{j,p} Y_{j,p}^b \frac{\Delta x_j}{\Delta x_i} \int_{x_{i-\frac{1}{2}}}^{p_i^j} b(x|x_j, p)\mathrm{d}x - S_{i,p} n_{i,p} Y_{i,p}^d, \end{aligned} \tag{24}$$

where $n_{i,p}$ is a two dimensional cell average, $F_{i,p\pm1/2}$, $F_{i\pm1/2,p}$ and $\Lambda_{i,p\pm1/2}$, $\Lambda_{i\pm1/2,p}$ are the convective and diffusional numerical fluxes at the upper/lower and left/right faces of (i,p)th cell, respectively. Fig. 1 represented these fluxes and the grid used in this study graphically.

3.5. Mass conservation and number preservation properties in the presence of nucleation, growth and growth rate dispersion

Here we are concerned with whether or not the mass conservation and number preservation properties of the WFV and MCNP schemes are still maintained in the presence of the discretized growth terms. Since the aggregation and fragmentation terms are already discussed above, we only consider the population balance equation with growth, growth rate dispersion and nucleation terms here:

$$\frac{\partial n}{\partial t} = -\frac{\partial (v_G n)}{\partial x} + D_g \frac{\partial^2 n}{\partial x^2}. \tag{25}$$

Integrating over x results in

$$\frac{\partial M_j}{\partial t} = -\int_{x_c}^{\infty} x^j \frac{\partial (v_G n)}{\partial x}\mathrm{d}x + D_g \int_{x_c}^{\infty} x^j \frac{\partial^2 n}{\partial x^2}\mathrm{d}x. \tag{26}$$

We integrate by parts to obtain

$$\begin{aligned} \frac{\partial M_j}{\partial t} &= \left(-x^j v_G n\Big|_{x_c}^{\infty} + \int_{x_c}^{\infty} j x^{j-1} v_G n\mathrm{d}x \right) \\ &+ D_g \left(x^j \frac{\partial n}{\partial x}\Big|_{x_c}^{\infty} - j x^{j-1} n\Big|_{x_c}^{\infty} + \int_{x_c}^{\infty} j(j-1) x^{j-2} n\mathrm{d}x \right). \end{aligned} \tag{27}$$

When $j = 0$ and $j = 3$, the analytical zeroth and third order moments are

$$\frac{\partial M_0}{\partial t} = -v_G n + D_g \frac{\partial n}{\partial x}\Big|_{x_c}^{\infty}, \tag{28}$$

$$\begin{aligned} \frac{\partial M_3}{\partial t} &= -x^3 v_G n + x^3 D_g \frac{\partial n}{\partial x} + 3 D_g x^2 n\Big|_{x_c}^{\infty} \\ &+ \int_{x_c}^{\infty} (3x^2 v_G n + 6x D_g n)\mathrm{d}x. \end{aligned} \tag{29}$$

Incorporating the nucleation and regularity boundary conditions, the above equations become:

$$\frac{\partial M_0}{\partial t} = B_0, \tag{30}$$

$$\begin{aligned} \frac{\partial M_3}{\partial t} &= B_0 x_c^3 + 3 D_g x^2 n\Big|_{x_c}^{\infty} + \int_{x_c}^{\infty} (3x^2 v_G n + 6x D_g n)\mathrm{d}x \\ &\approx B_0 x_c^3 + 3 D_g (x_{max}^2 n_{N_x} - x_c^2 n_1) + \sum_{i=1}^{N_x} (3x_i^2 v_{G,i} n_i \Delta x_i + 6 x_i D_g n_i \Delta x_i). \end{aligned} \tag{31}$$

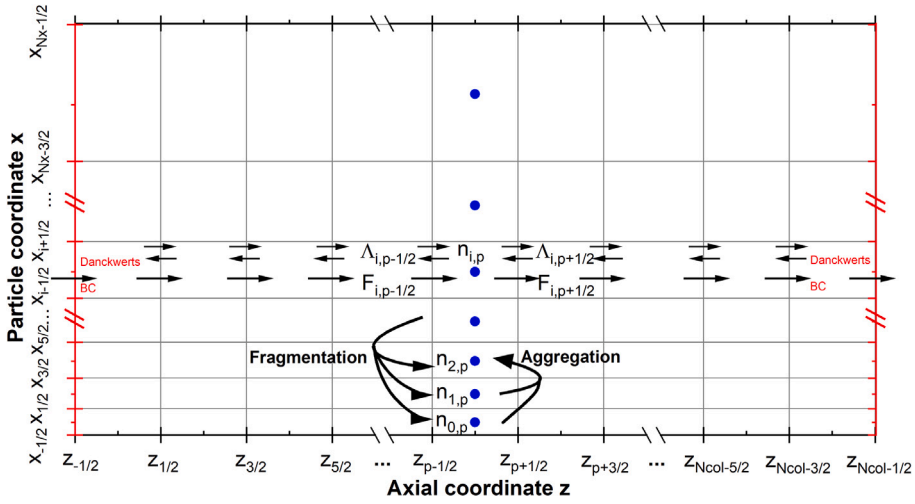

Fig. 1. Regular quadrilateral grid for 2D cell-centered FVM flux reconstruction. Axial convection fluxes at cell faces are unidirectional and denoted by longer arrows. Axial dispersion fluxes are bidirectional and denoted by smaller double arrows.

If the numerical discrete zeroth or third order moment is equivalent to the above equations, then the zeroth or third order moment is preserved.

The FVM discretized equation (25) is

$$\frac{\partial n_i}{\partial t} = -\frac{F_{i+1/2} - F_{i-1/2}}{\Delta x_i} + \frac{\Lambda_{i+1/2} - \Lambda_{i-1/2}}{\Delta x_i}. \tag{32}$$

As discussed in detail in Zhang et al. (2024), cells near the domain boundaries were treated differently by reducing the order of the numerical scheme. Therefore, the discrete j^{th} order moment M_j^{Δ} can be obtained by multiplying the above equation by $x_i^j \Delta x_i$ and summing over all cells:

$$\frac{\partial M_j^{\Delta}}{\partial t} = \sum_{i=1}^{N_x} -(F_{i+1/2} - F_{i-1/2})x_i^j + \sum_{i=1}^{N_x}(\Lambda_{i+1/2} - \Lambda_{i-1/2})x_i^j. \tag{33}$$

Recall that at the boundaries, $F_{1/2} - \Lambda_{1/2} = B_0$ and $F_{N_x+1/2} - \Lambda_{N_x+1/2} = 0$, and we obtain for the zeroth and third order moments

$$\frac{\partial M_0^{\Delta}}{\partial t} = F_{1/2} - \Lambda_{1/2} - (F_{N_x+1/2} - \Lambda_{N_x+1/2}) = B_0, \tag{34}$$

$$\frac{\partial M_3^{\Delta}}{\partial t} = B_0 x_c^3 + \frac{1}{2}\sum_{i=1}^{N_x-1}(\Delta x_i + \Delta x_{i+1})(x_i^2 + x_i x_{i+1} + x_{i+1}^2)(\Lambda_{i+1/2} - F_{i+1/2}). \tag{35}$$

Regarding the zeroth order moment, comparing Eqs. (30) and (34), we conclude that the zeroth order moment is preserved, independent of the definitions of $F_{i+1/2}$ and $\Lambda_{i+1/2}$.

Regarding the third order moment, comparing Eqs. (31) and (35), we conclude that for the numerical fluxes $F_{i+1/2}$ and $\Lambda_{i+1/2}$ defined in Zhang et al. (2024), the third order moment is not conserved.

As mentioned above, we enforce the nucleation source term through the boundary conditions and it thus does not influence the mass conservation or number preservation properties of the WFV or MCNP schemes in this case.

3.6. Mass conservation and number preservation properties for 2D cases

For 2D cases, the moments of the 2D distribution are also two-dimensional. Here we define the combined continuous j^{th} order moment w.r.t. x and k^{th} order moment w.r.t. z as:

$$M_{j,k} = \int_0^L \int_{x_c}^{x_{\max}} n x^j z^k \mathrm{d}x\mathrm{d}z. \tag{36}$$

By definition, the total count of the particles in the reactor is $M_{0,0}$ and the total volume or mass of particles in the reactor is $M_{3,0}$. That is, we only consider the zeroth order moment w.r.t. z. Note that at the reactor outlet, the distribution n is still one-dimensional.

To study the zeroth order moment w.r.t. z, consider the following convection–dispersion equation:

$$\frac{\partial n}{\partial t} = -v_{ax}\frac{\partial n}{\partial z} + D_{ax}\frac{\partial^2 n}{\partial z^2}. \tag{37}$$

A similar analysis as in the last section can be performed and M_0 is expressed as

$$\frac{\partial M_0}{\partial t} = v_{ax} n_{in} - (v_{ax} n)|_{z=L}, \tag{38}$$

where L is the length of the reactor. The discretized Dankwerts boundary conditions are: $F_{0.5} - \Lambda_{0.5} = v_{ax} c_{in}$ and $\Lambda_{N_z+0.5} = 0$. Therefore we obtain:

$$\frac{\partial M_0^{\Delta}}{\partial t} = v_{ax} n_{in} - F_{N_{col}+1/2}. \tag{39}$$

Comparing the above two equations, as $F_{N_{col}+1/2}$ is only an approximation to $(v_{ax} n)|_{z=L}$, we conclude that the zeroth order moment is not conserved due to the boundary condition of the DPFR. This result is expected as FVM are mass conserving in the sense that the zeroth order moment is preserved for intermediate cells but not necessarily at the domain boundaries (see e.g. LeVeque, 2002). Therefore, we conclude that neither $M_{0,0}$ nor $M_{3,0}$ are conserved for 2D cases.

4. Time integrator

As outlined in Zhang et al. (2024), we use a variable-step/variable-order backward differential formula (BDF) ODE integrator that is implemented in the implicit differential–algebraic solver (IDAS) package in the suite of non-linear and differential–algebraic equation solvers (SUNDIALS) (Hindmarsh et al., 2005) as the time integrator. During each time step, a Jacobian matrix is required by IDAS. CADET can generate this Jacobian using algorithmic differentiation (AD) in forward mode as implemented in a previous release (Püttmann et al., 2016). However, repeatedly computing the Jacobian using AD, and storing and carrying it over in the computer memory slows down the simulations. To reduce the runtime, we provide the solver with an analytical Jacobian.

We report the Jacobian entries for the 1D WFV schemes as:

$$\frac{\partial G_i}{\partial n_j} = \sum_{j,k\in A^i}^{k\geq j} \left(1 - \frac{1}{2}\delta_{j,k}\right) \beta_{jk} n_k \frac{\Delta x_j \Delta x_k}{\Delta x_i} \frac{x_j^3 + x_k^3}{2x_i^3 - x_j^3 - x_k^3},$$
$$\frac{\partial G_i}{\partial n_i} = -\sum_{j=1}^{N_x} \beta_{ij} n_j \Delta x_j \frac{x_{l_{ij}}^3}{2x_{l_{ij}}^3 - x_i^3 - x_j^3}, \quad \frac{\partial G_i}{\partial n_j} = -\beta_{ij} n_i \Delta x_j \frac{x_{l_{ij}}^3}{2x_{l_{ij}}^3 - x_i^3 - x_j^3}, \tag{40}$$

where the first equation provides the Jacobian elements for the source term, with symmetric j and k, and the second equation provides the elements for the sink term. The Jacobian entries for the MCNP scheme are given by:

$$\frac{\partial G_i}{\partial n_j} = S_j Y_j^b \frac{\Delta x_j}{\Delta x_i} \int_{x_{i-\frac{1}{2}}}^{p_i^j} b(x|x_j)\mathrm{d}x,\ j \in [i, N_x), \qquad \frac{\partial G_i}{\partial n_i} = S_i Y_i^d, \tag{41}$$

where the first equation is used for the source term and the second equation is used for the sink term. The correctness of the Jacobian implementation was verified by comparison with an AD Jacobian.

5. Numerical case studies

We validate the particle size based WFV and MCNP schemes and their implementations for aggregation and fragmentation processes by comparing numerical results with reference solutions for analytically tractable kernels. We also present several cases where aggregation and fragmentation are combined with the nucleation, growth and growth rate dispersion terms solved in our part I work. Convergence rates and runtimes were determined and analyzed. Zeroth to sixth order moments were also compared. This range covers all moments of practical importance. Here, the volume-averaged mean size is defined as the ratio of the fourth to third order moment (M_4/M_3).

For these numerical case studies, the upper boundary is truncated from infinity to a finite but sufficiently large particle size. For pure aggregation, we are concerned with particularly hard test cases with aggregation levels $I_{agg} \geq 95\%$, representing a reduction of the total number of the particles is below 5% of the initial number at specific times, where I_{agg} is defined by

$$I_{agg} = 1 - \frac{M_0}{M_0(t=0)}. \tag{42}$$

For comparison, we define a dimensionless p^{th} order moment $\overline{M_p}$ by: $\overline{M_p} = M_p/M_p(t=0)$. In the literature, initial conditions and analytical solutions are mostly reported with particle volume as the internal coordinate. In the following, these solutions are converted to a size-based form using Eq. (1). If not otherwise stated, both the IDA absolute and relative tolerances are set to 10^{-6}. Logarithmic (base 10) and uniform grids are used for the discretization of the internal and external coordinates x and z. All tests and benchmarks are performed on a 3600 MHz AMD Ryzen(TM) Threadripper(TM) with 32 cores and 64 threads. Simulations were parallelized only for the 2D cases.

Normalized L^1 and L^∞ errors are given by

$$\varepsilon_{L^1} = \frac{\sum_{i=1}^{N_x} \Delta x_i |n_i^{(\text{numerical})} - n_i^{(\text{reference})}|}{\sum_{i=1}^{N_x} \Delta x_i n_i^{(\text{reference})}},$$

and

$$\varepsilon_{L^\infty} = \frac{\max_{1\leq i\leq N_x}(|n_i^{(\text{numerical})} - n_i^{(\text{reference})}|)}{\max_{1\leq i\leq N_x}(|n_i^{\text{reference}}|)}.$$

The L^1 experimental order of convergence (EOC) based on the internal coordinate x is defined as

$$\text{EOC} = \log_{N_x^{(\text{B})}/N_x^{(\text{A})}} \left(\frac{\varepsilon_{L^1}^{(\text{A})}}{\varepsilon_{L^1}^{(\text{B})}}\right).$$

The numerical case studies are organized as follows: cases 1 to 5 considered STR batch processes while case 6 to 9 considered DPFR processes. Case 5 and 9 combined our part I work to consider inclusion of nucleation and growth mechanisms for unified population balance modeling.

5.1. Case 1: Constant aggregation kernel in a BSTR

First, we consider a size-independent constant aggregation kernel with $\beta = \beta_0 = 1$. For a batch stirred tank reactor (BSTR) with initial condition

$$n(\text{t}=0) = 3x^2 \frac{N_0}{L_0^3} \exp\left(-\frac{x^3}{L_0^3}\right), \tag{43}$$

(Scott, 1968) provided an analytical solution:

$$n = \frac{12 N_0 x^2}{L_0^3 (Y+2)^2} \exp\left(\frac{-2x^3}{L_0^3 (Y+2)}\right),$$

where $Y = N_0 \beta_0 t$. N_0 and L_0 are the initial number of particles and the initial mean size, respectively. Hounslow et al. (1988) provided an analytical solution for the six leading dimensionless moments:

$$\overline{M_p} = \left(\frac{2}{2+Y}\right)^{1-p/3}.$$

The parameter values used are reported in Table S2.

Fig. 2(a) shows the numerical and analytical solutions that are in excellent agreement. Compared to the situation at $t = 1$ s, at $t = 4$ s there are more larger particles, which is expected for aggregation processes. The aggregation level I_{agg} increased from 0.83 to 0.95 as time elapsed from 1 s to 4 s, indicating the total count of the particles are reduced by another 12%. Note that accurate estimates of I_{agg} depend on accurate calculations of the total particle count, which underlines the importance of preserving the zeroth order moment with the WFV scheme. Figure S2 shows absolute errors between the numerical solutions and analytical solutions. Compared to the parts where the distribution is nearly zero-valued, larger errors are observed where the distribution values are also large.

To evaluate the accuracy of the moments, numerical and analytical moments up to sixth order were plotted in Fig. 2(c) and (d) and the normalized L^∞ error (ε_{L^∞}) of these moments is reported in the inset of (d). Even for the $I_{agg} = 0.95$ case, the ε_{L^∞} errors for the leading sixth moments are small: the zeroth to fourth moments show errors below 0.5 percent while the errors of the fifth and sixth moments are below 2.5 percent. The zeroth and third order moments are of special interest as they are preserved and conserved, according to Propostions 1 and 2, respectively. The ε_{L^∞} error of the third order moment is 8.9×10^{-14}, which is practically zero, validating our theory and implementation. Minor errors are seen for the zeroth order moments, which can be attributed to a truncation error in the sink term in Eq. (19): indices l_{jk} outside the domain boundary ($x_{max} = 100$ μm) for mother particles of large sizes are not counted in the sink term, which causes an imbalance between the aggregation source and sink terms. This explanation was verified by increasing x_{max} to 500 while keeping a constant relative cell size by increasing $N_x = 500$. The zeroth order moment ε_{L^∞} decreased from to 6.9×10^{-4} to 5.3×10^{-5}. Further, despite the fact that the preservation of other order moments is not theoretically guaranteed, the proposed scheme captures them accurately with errors smaller than 2.5% on a grid with a modest number of cells $N_x = 100$.

Unfortunately, a theoretical analysis of the convergence rate of the WFV scheme is not available in the literature and is out of the scope of this study. Hence, we only report the experimental convergence rate. Fig. 2(b) shows the normalized L^1 error as a function of the number of cells N_x. The slope representing the EOC was found to be 1.9. This aligns with our expectation, as the dominating approximation made by the schemes is the second order midpoint quadrature rule. Regarding the runtime (Figure S1), we found it to increase at an order

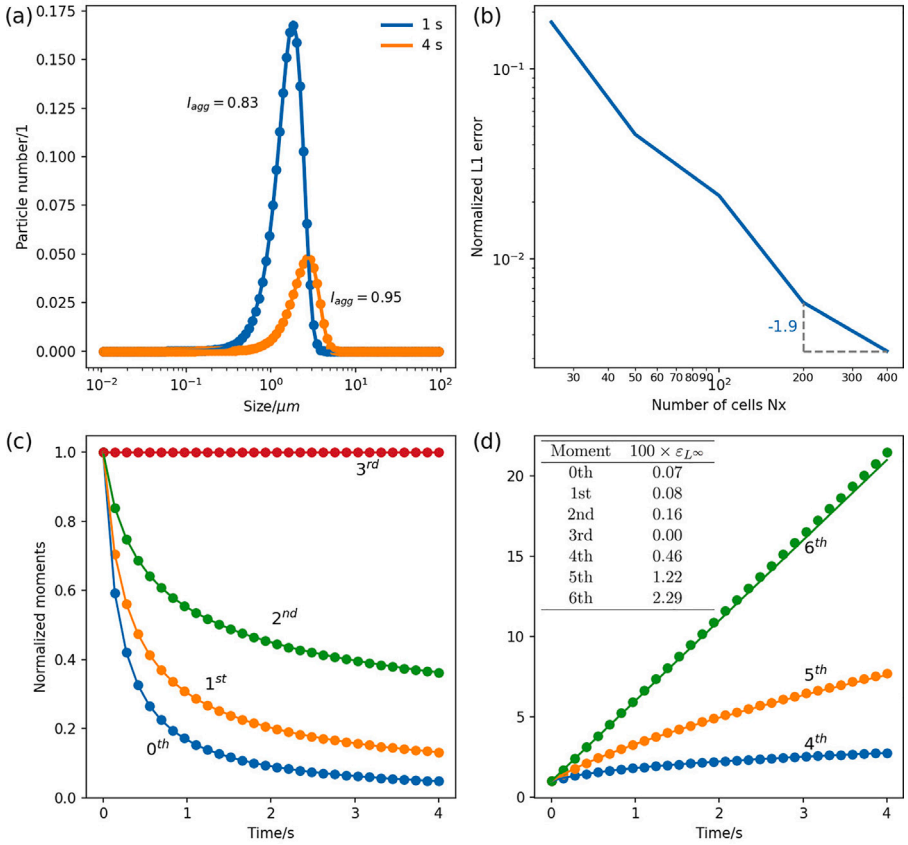

Fig. 2. Case 1: constant aggregation kernel with 100 logarithmic cells. Dotted and solid curves are numerical and analytical solutions, respectively. Moments and convergence rate were calculated at $t = 4$ s. (a) Numerical and analytical solutions; (b) convergence analysis; (c) zeroth to third order dimensionless moments; (d) fourth to sixth order dimensionless moments.

of about 3 when N_x is increased, indicating a high computational burden. A possible explanation is that the number of combinations j and k belonging to set A^l increased rapidly as the grid resolution increased, leading to many more combinations of j and k and the observed runtime overhead.

5.2. Case 2: Golovin aggregation kernel in a BSTR

In this case, we test our implementation for aggregation with the size dependent Golovin kernel $\beta = \beta_0(x_j^3 + x_k^3)$. For a BSTR with the same initial condition as in the first case, Eq. (43), the 1D Smoluchowski coagulation equation has an analytical solution (Lister et al., 1995):

$$n = \frac{3N_0(1-T)}{xT^{0.5}} \exp\left(-(1+T)\frac{x^3}{L_0^3}\right) I_1\left(\frac{2x^3}{L_0^3}T^{0.5}\right),$$

where $T = 1 - \exp(-Y)$ and $Y = N_0 L_0^3 \beta_0 t$. I_1 is the modified Bessel function of the first kind of order one. The parameter values used are reported in Table S1.

Fig. 3(a) shows the numerical and analytical solutions, which were in excellent visual agreement with each other. The EOC was found to be 1.2% in Fig. 3(b), which is smaller than that in the constant kernel case. This might be due to the asymptotic nature of numerical convergence, i.e. the theoretical order of convergence might only be achieved for a large number of cells which results in excessive computational demand. We consider further numerical studies to be worthwhile only after a theoretical order analysis has been derived, which is not yet available for the WFV. Similar to case 1, larger errors are observed for the parts of the distribution where the absolute values are also higher (Figure S4). The runtime also increased at a rate of about 3.0 with increasing N_x (Figure S3).

5.3. Case 3: Binary fragmentation with linear selection function in a BSTR

In this case study, we test our algorithm and implementation for the size-based MCNP scheme. Consider uniform particle binary breakage ($\gamma = 2$) with a linear selection function ($\alpha = 1$, $S_0 = 1$) with respect to the particle volume: $b(x|\lambda) = 6x^2/\lambda^3, S = x^3$. $N_j = 2$ indicates that a mother particle breaks up into two daughter particles on average. For this distribution $b(x|\lambda)$, the integral in Eq. (20) can be solved analytically:

$$\int_{x_{i-\frac{1}{2}}}^{p_i^j} b(x|x_j)\mathrm{d}x = \int_{x_{i-\frac{1}{2}}}^{p_i^j} \frac{6x^2}{x_j^3}\mathrm{d}x = \frac{2\left((p_i^j)^3 - x_{i-\frac{1}{2}}^3\right)}{x_j^3}.$$

In a BSTR with initial condition given by Eq. (43), $N_0 = 1$ and $L_0 = 1$, the fragmentation equation has an analytical solution (Hounslow et al., 2001):

$$n = 3x^2(1+t)^2 e^{-x^3(1+t)}.$$

(Peterson, 1986) has provided analytical solutions for the dimensionless p^{th} moments $\overline{M_p}$:

$$\overline{M_p} = \left(1 + \left(\frac{\Gamma(\frac{\gamma-1}{\alpha})}{\Gamma(\frac{\gamma}{\alpha})}\right)^{\alpha} \tau\right)^{\frac{3-p}{3\alpha}},$$

where Γ is the gamma function and τ is the dimensionless time defined by $\tau = S_0\left(\frac{M_3}{M_{0(t=0)}}\right)^{\alpha} t$.

Fig. 4(a) shows the numerical and analytical results. Compared to the solution at $t = 1$ s, the distribution at $t = 4$ s describes a larger total number of particles but with a lower average size, indicative of a fragmentation process. Similar to the aggregation cases, larger errors

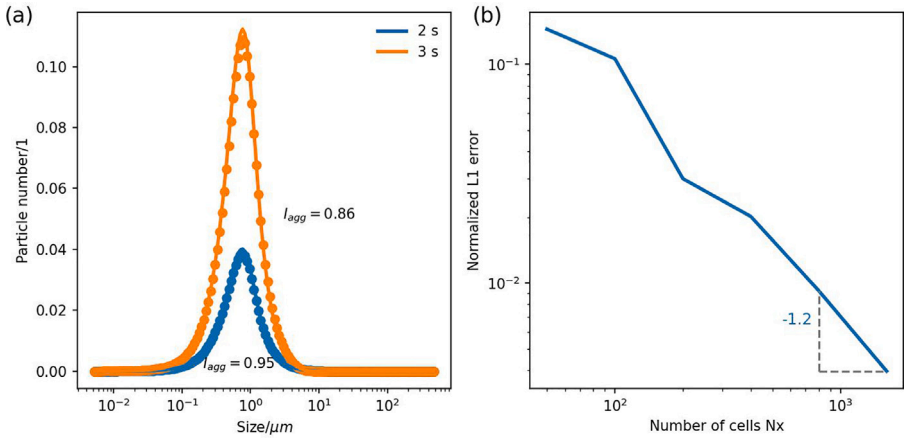

Fig. 3. Case 2: Golovin aggregation kernel with 150 logarithmic cells. Dotted and solid curves are numerical and analytical solutions, respectively. Moments and convergence rate were calculated at $t = 3$ s. (a) Numerical and analytical solutions; (b) convergence analysis.

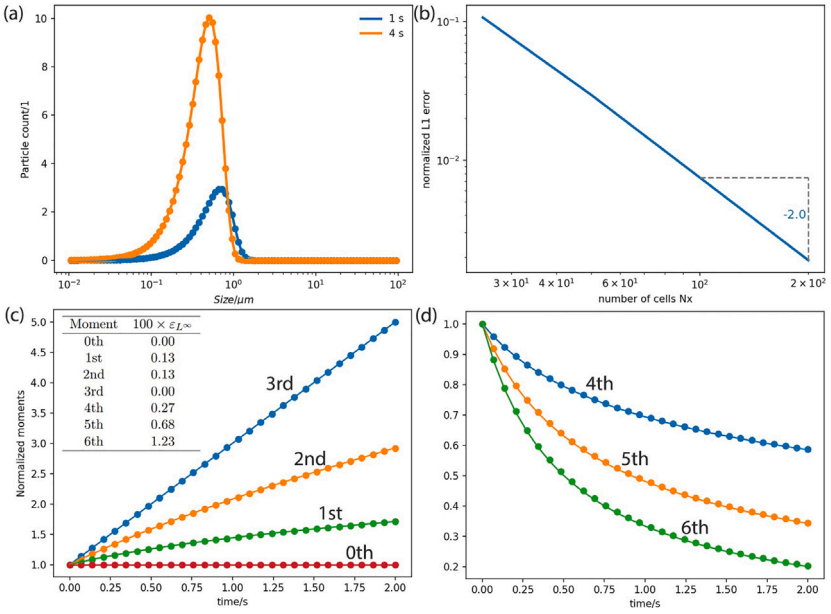

Fig. 4. Case 3: binary fragmentation with linear selection function and 100 logarithmic cells. Dotted lines are numerical solutions and solid lines are analytical solutions. (a) Numerical and analytical solutions; (b) convergence analysis; (c) zeroth to third order dimensionless moments; (d) fourth to sixth order dimensionless moments.

were observed for the parts of the distributions where their absolute values are also large (Figure S4). As shown in Fig. 4(c) and (d), all moments were accurately tracked with the largest error of 1.23% in the sixth order moment. According to Propositions 3 and 4, the zeroth and third order moments should be preserved and conserved, respectively. When $N_x = 100$, the ε_{L^∞} errors for both moments are 8.0×10^{-7} and 1.6×10^{-9}, respectively, which verifies the size-based MCNP scheme and its implementation. Fig. 4(b) shows an EOC of 2.0, which is again expected. Here, the runtime increased at a rate of approximately 2.0 with increasing N_x, which was expected to be lower compared to the aggregation simulations since the costly computation of A^l is not required in the fragmentation case.

5.4. Case 4: Simultaneous aggregation and fragmentation in a BSTR

In this case, the Smoluchowski coagulation equation (2) and fragmentation equation (6) are solved simultaneously. This setup does not necessarily yield equilibrium solutions for all combinations of aggregation and fragmentation kernels and selection functions (Vigil, 2009). We refer to Vigil (2009), Sorensen et al. (1987) and Vigil and Ziff (1989) for details and necessary conditions for equilibrium solutions, and note that equilibrium solutions exist particularly when constant aggregation kernels are coupled with linear selection functions and binary fragmentation. In this case, (Patil and Andrews, 1998) provided an analytical solution which was later simplified by Lage (2002). The kernels are: $\beta = \beta_0 = 0.2$, $S(x) = S_0 x^3 = 0.1x^3$, $b(x|\lambda) = 6x^2/\lambda^3$. In a BSTR with initial condition

$$n = 3M_0(\mathrm{t}=0)\left(\frac{2M_0(\mathrm{t}=0)}{M_3}\right)^2 x^5 \exp\left(-\frac{2M_0(\mathrm{t}=0)}{M_3}x^3\right),$$

and when the condition $2S_0M_3 = \beta_0(M_0(\mathrm{t}=0))^2$ is fulfilled, the analytical solution is:

$$n = \frac{3(xM_0(\mathrm{t}=0))^2}{M_3}\sum_{i=1}^{2}\frac{K_1 + p_i K_2}{L_2 + 4p_i}\exp(p_i\eta),$$

where K_1, K_2, p_i, L_2 and η are defined in the supplementary material section 1.

Fig. 5(a) shows the transient behavior of this process. First, the fragmentation dominated the aggregation process which led to an increase in the number of small particles and the disappearance of

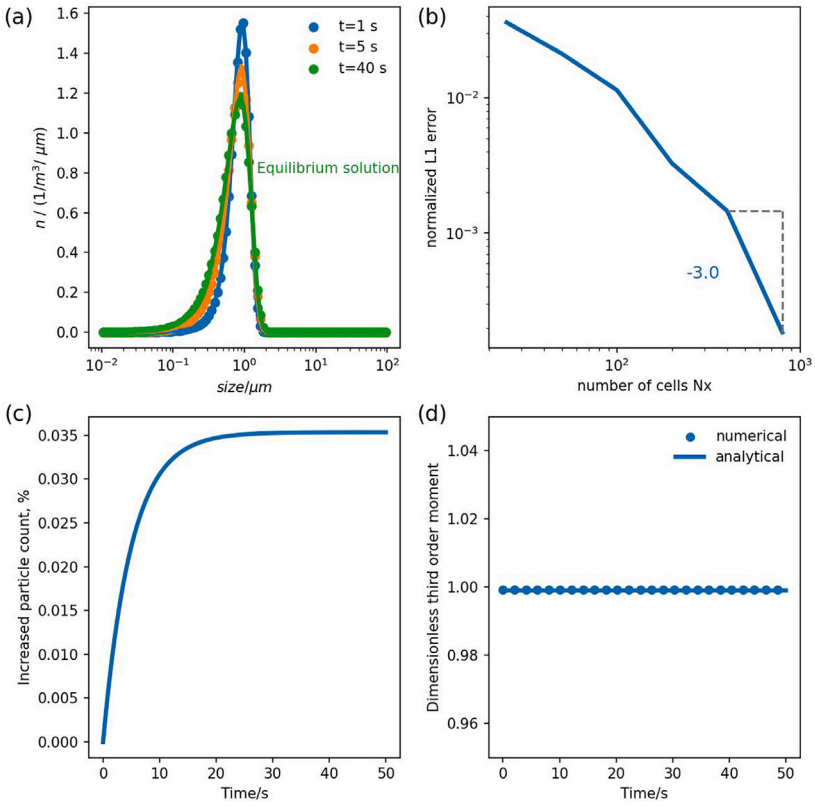

Fig. 5. Case 4: simultaneous aggregation and fragmentation. (a) Numerical and analytical solutions at different times; (b) convergence analysis at t = 40 s; (c) total particle count in the system changes as a function of time; (d): numerical and analytical third order moments.

larger particles. As time elapsed, the increasing aggregation rate of small particles eventually matched the fragmentation rate, leading to an equilibrium distribution. The duration of the equilibration process depends on the rate constants of both the aggregation and fragmentation processes. The equilibration dynamics are also reflected in Fig. 5(c), which describes the evolution of the total particle count in the system. The total particle count increased until the aggregation rate matched the fragmentation rate. A constant total particle count is an important indicator of whether or not an equilibrium state is reached, which again underlines the importance of preserving the zeroth order moment in the WFV and MCNP schemes. Fig. 5(b) shows the EOC to be 3.0 on a logarithmic grid, which is higher than previous cases where aggregation and breakage were considered separately. The fact that convergence is an asymptotic property is most certainly the reason for the EOC exceeding the expected rate of 2.0. As shown in Figure S7, the runtime increased at a rate of around 3.0 with increasing N_x, which is expected as the aforementioned computational demands of aggregation are dominating. The analytical and numerical third order moments are compared in Fig. 5(d). As expected, it is still conserved with $\epsilon_{L^\infty} = 2.9 \times 10^{-4}$ when aggregation and fragmentation are simultaneously considered, validating our implementation.

5.5. Case 5: Size-dependent growth and constant aggregation kernel in a BSTR

Consider a case where size-dependent growth and aggregation with a constant kernel ($\beta = \beta_0$) take place simultaneously in a BSTR. If the growth rate is proportional to the particle volume: $v_G = \sigma v$, where $\sigma > 0$ is a constant, the volume-based governing equation reads:

$$\frac{\partial n_v}{\partial t} = -\sigma \frac{\partial (v n_v)}{\partial v} + \frac{1}{2}\int_0^v \beta(v-\tilde{v},\tilde{v}) n_v(v-\tilde{v}) n_v(\tilde{v}) \mathrm{d}\tilde{v} - n_v(v)\int_0^\infty \beta(v,\tilde{v}) n_v(\tilde{v}) \mathrm{d}\tilde{v}.$$

The above volume-based equation can be converted to the following size-based equation with details provided in the supplementary material:

$$\frac{\partial n}{\partial t} = -\frac{\sigma}{3}\frac{\partial (xn)}{\partial x} + \frac{x^2}{2}\int_0^x \frac{\beta\left((x^3-\lambda^3)^{\frac{1}{3}},\lambda\right)}{(x^3-\lambda^3)^{\frac{2}{3}}} n\left((x^3-\lambda^3)^{\frac{1}{3}}\right) n(\lambda)\mathrm{d}\lambda - n\int_0^\infty \beta(x,\lambda) n(\lambda)\mathrm{d}\lambda.$$

Note the change of σ to $\sigma/3$. This system has an analytical solution for the initial condition (Eq. (43)):

$$n = 3x^2 \frac{M_0^2}{M_3} \exp\left(-\frac{M_0}{M_3} x^3\right),$$

where $M_0 = 2N_0/(2+\beta_0 N_0 t)$ and $M_3 = N_0 x_0^3 \exp(\sigma t)$. M_0 and M_3 are also the analytical solutions of the zeroth and third order moments. Model parameters are reported in Table S4.

Fig. 6(c) shows the analytical and numerical solutions. The numerical solutions with the growth term reconstructed using both the HR Koren and WENO35 schemes are in excellent agreement with the analytical solution: a convergence analysis in Fig. 6(a) shows that both schemes started with approximately the same error, but the WENO35 scheme converged faster than the HR Koren scheme, both at a rate of approximately 2.0. This is expected, since the theoretical convergence rate of the HR Koren scheme is between 1.0 and 2.0. On the contrary, when the WFV scheme is combined with the WENO35 scheme, the overall EOC of 2.2 is below the theoretical convergence rate of the WENO35 scheme between 3.0 and 5.0. This is also expected as the lower order method always dominates the global rate, which is expected to be 2.0 for the WFV. Further taking the runtime into consideration, we found that the WFV scheme performed better when combined with the WENO35 scheme compared to the HR Koren scheme, as the former always achieved a lower error for a given

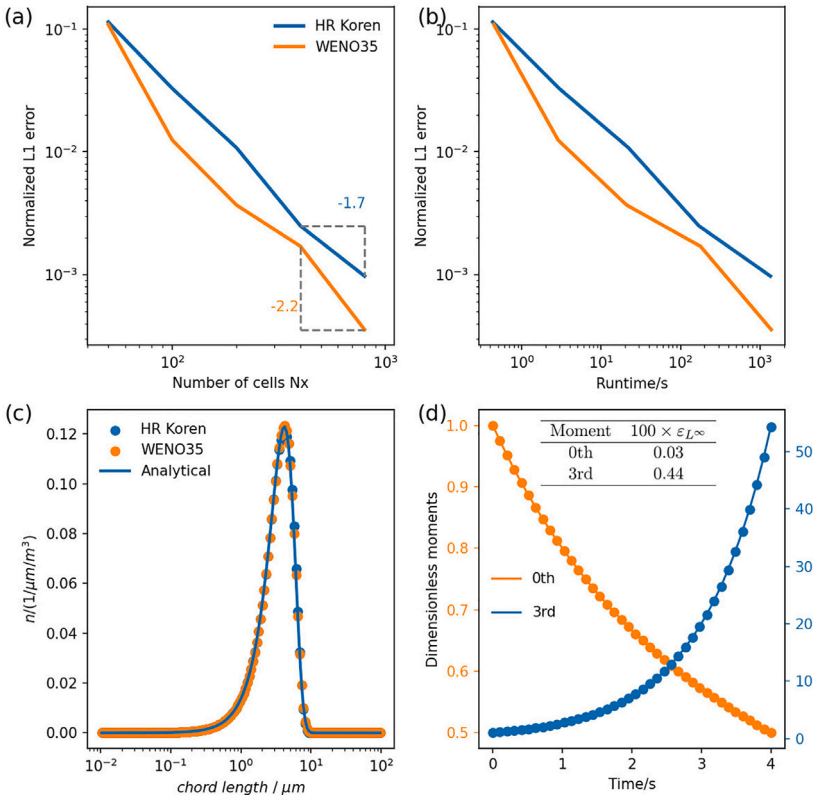

Fig. 6. Case 5: simultaneous growth and aggregation. (a) Convergence analysis; (b) error as a function of runtime; (c) numerical and analytical solutions at $t = 4$ s with $N_x = 150$; (d) numerical (dots) and analytical (lines) zeroth and third order moments with $N_x = 150$.

runtime. As shown in Figure S8, we found that the runtime increased at a rate of around 3.0 when N_x was increased, which is again dominated by the computational demands of aggregation.

Since growth terms are present in this 1D case, as discussed in Section 3.5, the zeroth order moment is still preserved, but the third order moment is no longer strictly conserved. In Fig. 6(d), when comparing the numerical moments with the analytical moments, we found that the ε_{L^∞} error was negligibly small (3.2×10^{-4}) for the zeroth order moment. The error of the third order moment, compared to case 1 where growth terms are absent and $\varepsilon_{L^\infty} = 8.9\times10^{-14}$, increased due to the presence of the growth term. However, the error was still small $\varepsilon_{L^\infty} = 4.4\times10^{-3}$. As expected, these errors can be further reduced by increasing N_x from 150 to 300: ε_{L^∞} for the zeroth and third order moment become 7.9×10^{-5} and 3.9×10^{-3}, respectively.

5.6. Case 6: Pure aggregation in a DPFR

In this case study, we consider pure aggregation in a DPFR with the governing equation (12) and a constant aggregation kernel. Nucleation, growth, growth rate dispersion, and breakage are disabled by setting $B_0 = v_G = S = D_g = 0$. The DPFR is initially devoid of particles, and particles with a log-normal size distribution are fed to the reactor:

$$n_{\text{feed}} = \frac{A}{\sqrt{2\pi}wx}\exp\left(\frac{-\ln^2(x/c)}{2w^2}\right), \tag{44}$$

where $A = 10^{16}$, $w = 0.4$ and $c = 20$. A uniform grid was used for the external coordinate and a logarithmic grid for the internal coordinate. An analytical solution is not available for this case. Hence, we used a numerical solution obtained on a fine grid (250×450) as reference solution. Each flux reconstruction scheme (HR Koren and WENO35) together with the WFV was benchmarked on 5 grid resolutions for the external coordinate and 5 grid resolutions for the internal coordinate, resulting in 25 combinations (Table S3). The axial velocity, dispersion coefficient, diameter and length of the reactor are specified in Table S6. They are configured such that the mean residence time in the reactor is about 85 s. The simulation time of 200 s suffices to obtain a steady-state solution.

Fig. 7(a) shows the solution at $t = 130$ s inside the reactor. As a result of aggregation, the number density distribution decreases along the axial position from the inlet to the outlet of the reactor.

The number of cells N_{col} along the axial coordinate z has a strong impact on the resulting distribution, as shown in Fig. 8(a). Compared to a BSTR ($N_{col} = 1$), the DPFR significantly sharpens the distribution for the same kinetic parameters. Further increasing N_{col} only slightly improved the approximation as shown in Fig. 8(b). This also justified why we chose a moderate value of $N_{col} = 250$ in the reference solution.

In Fig. 9(a), the scatter plot represents all the points tested for each reconstruction scheme. The Pareto fronts, indicated by the solid lines, mark the best combinations for discretization, meaning that they could achieve the best trade-off between approximation error and computation time. In this case, both HR Koren and WENO35 schemes performed similarly as their Pareto fronts are very close to each other. This is also reflected in Fig. 10 where the error decreases as a function of N_x and N_{col}. The overall EOC was found to be around 2.0 for both the HR Koren and WENO35 schemes. This is also expected as the feed (source) enters the system from the boundaries, limiting the axial FVM to second order convergence. Further, the WFV is also second order convergent. The projections of the Pareto fronts onto the N_x-N_{col} plane in Fig. 10 show that it is most efficient to increase N_x and N_{col} proportionally. This behavior is expected as otherwise the error in one coordinate dominates the approximation accuracy.

As depicted in Figure S9, the increase in required computational time was almost linear in both coordinates on a logarithmic scale, with the slope (rate) being 2.0 and 1.0 along the N_x and N_{col} axes, respectively, aligning with our previous observations.

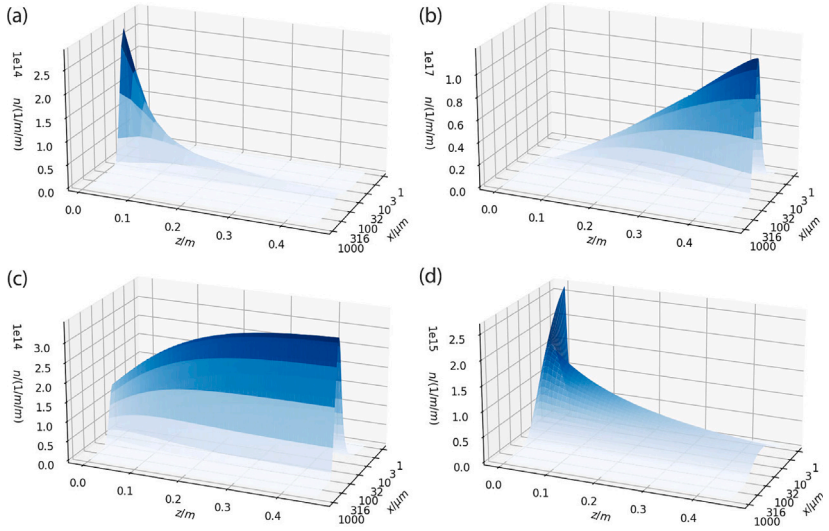

Fig. 7. Full solutions inside the DPFR on a 100 × 100 grid at $t = 130$ s. (a) Case 5: pure aggregation; (b) case 6: pure fragmentation; (c) case 7: simultaneous aggregation and fragmentation; (d) case 9: nucleation, growth, growth rate dispersion and aggregation.

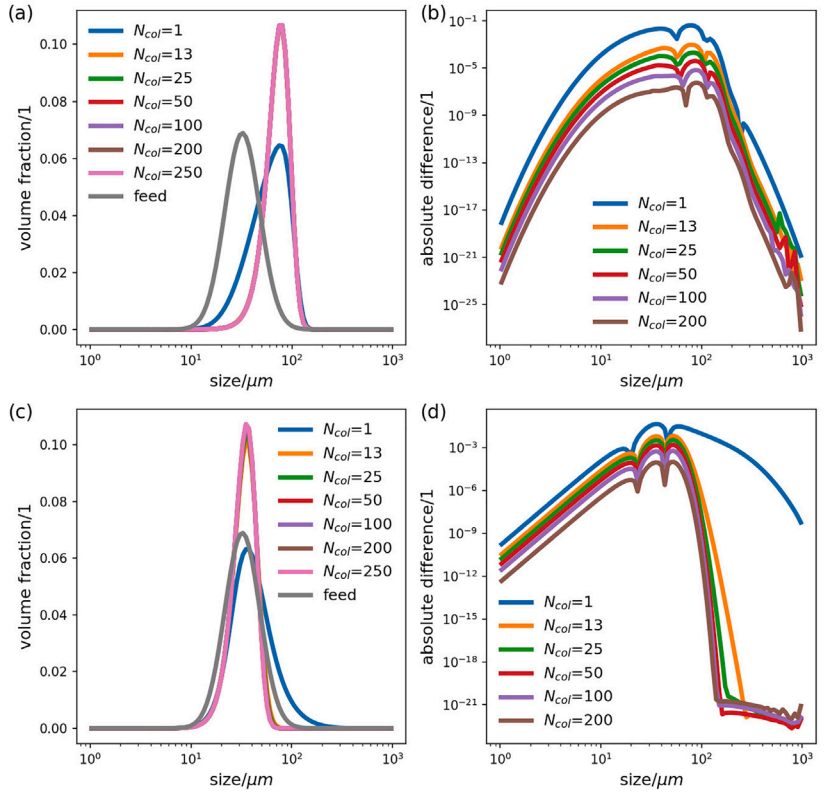

Fig. 8. Cases 6-7: aggregation or fragmentation in a DPFR. Impact of N_{col} on the simulated volume fractions obtained at the outlet of the reactor. (a) Case 5: pure aggregation; (c) case 6: pure fragmentation; (b) and (d): absolute differences between the numerical and analytical results. Curves corresponding to $N_{col} = 13 \sim 200$ are hidden behind $N_{col} = 250$ in (a) and (c) due to their small numerical differences seen in (b) and (d).

Furthermore, we compare moments $M_{0,0}$ and $M_{3,0}$ with a reference value to evaluate their preservation and conservation properties. In Fig. 11(a), when keeping N_x constant but varying N_{col}, the zeroth order moment varied dramatically such that the differences could be visually observed, indicating its non-preservation. In Fig. 11(b), when varying N_x, all approximations of $M_{0,0}$ remained invariant visually. Further plotting a normalized absolute difference in Figure S10, we notice that there are still errors for $M_{0,0}$. This is also expected as $M_{0,0}$ is not preserved for the entire reactor as it depends on both x and z, however, the errors are generally small ($< 0.6\%$) and the solution converges with increasing grid resolution. A similar analysis was performed for $M_{3,0}$ as shown in Fig. 11(c) and (d). Although the conservation of this moment is not theoretically guaranteed, its errors are small ($< 1.6\%$) and the solution converges with increasing grid resolution. The WENO35 scheme shows similar behavior as the HR Koren scheme and is omitted here.

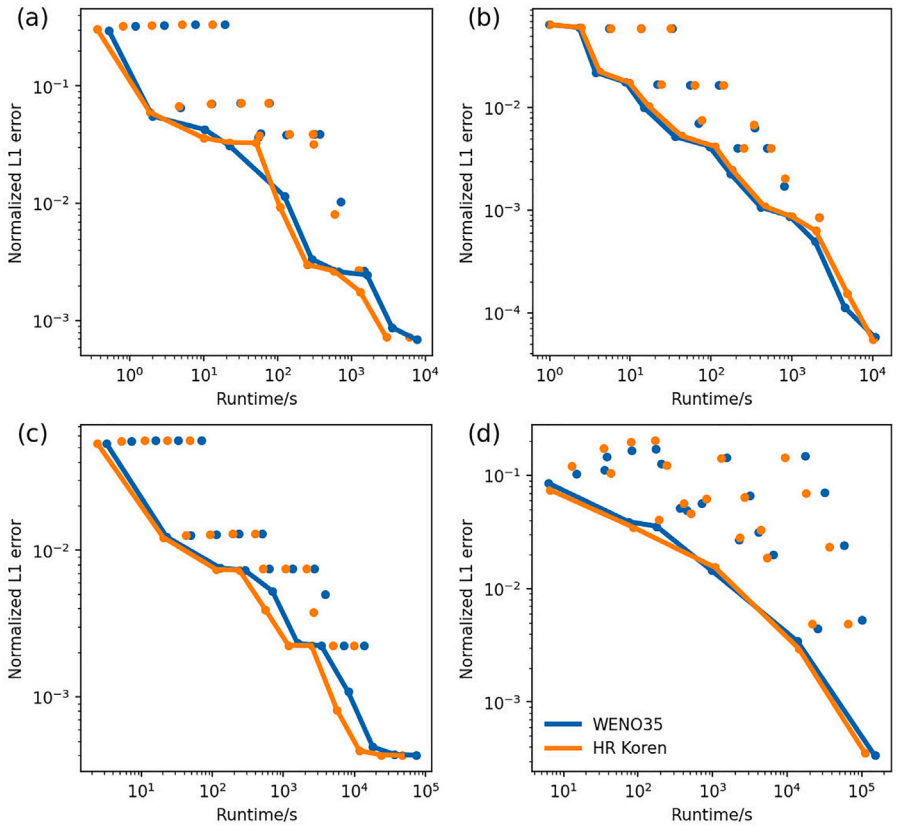

Fig. 9. Cases 6-9: normalized L^1 errors over runtime for DPFR cases. Points indicate tested combinations of grid resolution and the solid lines are Pareto fronts. (a) Case 6: pure aggregation; (b) case 7: pure fragmentation; (c) case 8: simultaneous aggregation and fragmentation; (d) case 9: nucleation, growth and aggregation.

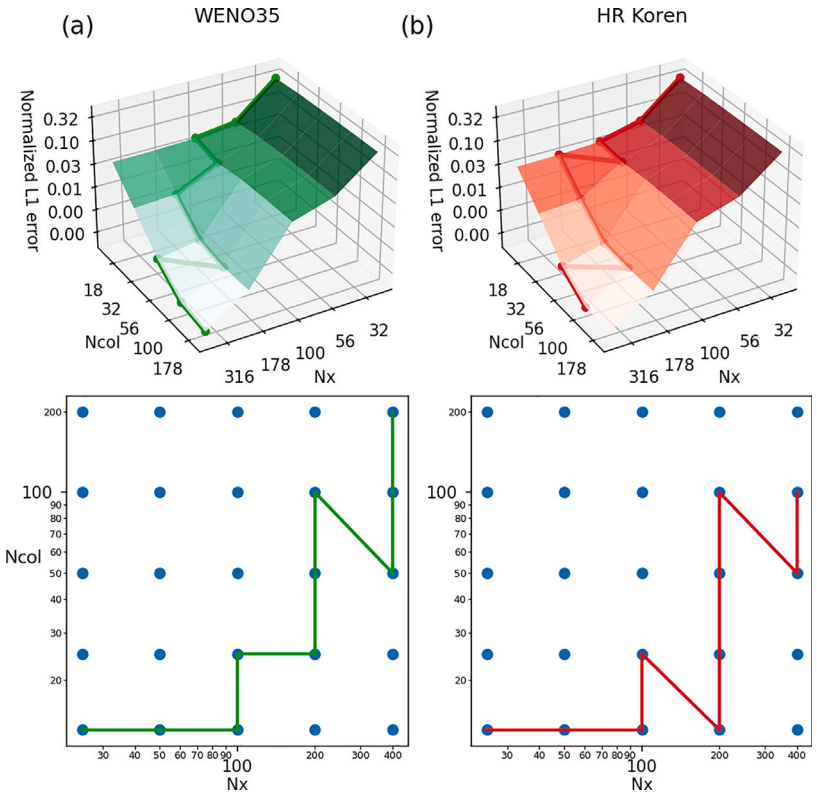

Fig. 10. Case 6: pure aggregation in a DPFR. Top: Normalized L^1 error as a function of N_x and N_{col}. Solid lines are the Pareto fronts. Bottom: projections of the Pareto fronts to the N_x-N_{col} plane. (a): WENO35; (b): HR Koren.

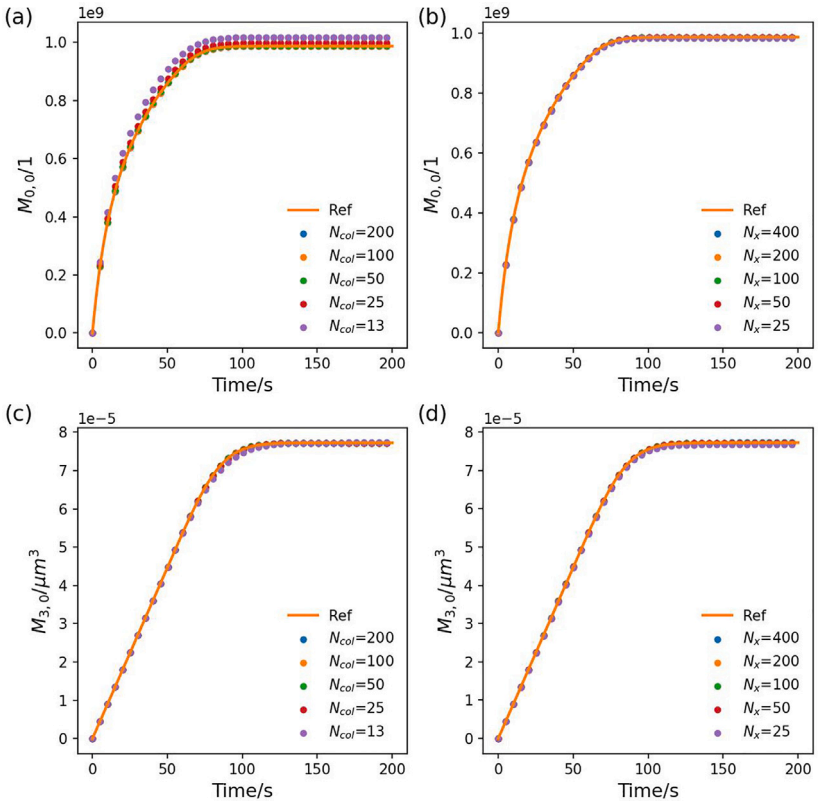

Fig. 11. Numerical and reference $M_{3,0}$ and $M_{0,0}$ for the entire reactor in case 6: (a): $M_{0,0}$ vs. N_{col}; (b): $M_{0,0}$ vs. N_x; (c): $M_{3,0}$ vs. N_{col}; (d): $M_{3,0}$ vs. N_x. Results were obtained using HR Koren scheme.

Lastly, in addition to the 2D moments, we also evaluated two important scalar metrics, the volume-averaged mean size and the total count of the particles, calculated from moments of the outlet distribution at steady state. Fig. 12 shows their relative errors as a function of N_x and N_{col}. The errors for these metrics were clearly decreasing when N_x and N_{col} were increased. The observed behavior is not surprising as neither of these metrics is guaranteed to be preserved. However, their errors were generally small, $\sim 1\%$, even on coarse grids.

5.7. Case 7: Pure fragmentation in a DPFR

In this case study, we consider a fragmentation process in a DPFR with governing equation (12). A linear selection function and binary particle fragmentation, the same as in case 3, are considered. Nucleation, growth, growth rate dispersion, and aggregation are disabled by setting $B_0 = v_G = S = \beta = 0$. The DPFR is free of particles initially and particles with a seed distribution according to Eq. (44) are fed into the reactor at the inlet. The testing procedure is the same as described in the previous case. Further model parameters are given in Table S5 and Table S7.

A full solution is shown in Fig. 7(b). As a natural result of the fragmentation, the area under the distribution increases towards the outlet of the reactor. The influence of N_{col} on the accuracy of the numerical solution at the reactor outlet is depicted in Fig. 8(c). Similar to the above case, except for $N_{col} = 1$, increasing N_{col} only slightly improved the solution (Fig. 8(d)).

As shown in Fig. 9(b), both the WENO35 and HR Koren schemes had similar performance with an overlap in their Pareto fronts, indicating that a similar error can be achieved in similar compute time. When the Pareto fronts are projected onto the N_x-N_{col} plane (Figure S12), we found that increasing N_x and N_{col} proportionally is an efficient method to stay on the Pareto fronts for the same reason explained in the previous case. Further, errors decreased at a rate of approximately 2 along both the N_x and N_{col} axes. The runtime depicted in Figure S11 increased at a first order rate when increasing N_{col} while a rate of two was observed when increasing N_x. A rate of approximately 2 is likely due to the rapid increase in the number of iterations for j to compute the modification factors in the MCNP scheme (21) as N_x (or i) increased. These observations were similar to those for the pure aggregation in DPFR case.

Lastly, the moments $M_{0,0}$ and $M_{3,0}$ are evaluated in Figure S14 and their normalized absolute error is plotted in Figure S15. Similar to the last test case, despite the fact that they are not strictly preserved, the errors are small even on a coarse grid ($< 3.5\%$) and exhibit convergent behavior when the grid resolution improves. Regarding the mean size and the total count at the reactor outlet (Figure S13), all errors were also very small ($< 1\%$) and converged with increasing N_x or N_{col}.

5.8. Case 8: Simultaneous aggregation and fragmentation in a DPFR

In this case study, we consider an aggregation-fragmentation equilibrium in a DPFR. The ratio of the aggregation and fragmentation rate constants ($\beta_0 = 2.4 \times 10^{-12}$, $S_0 = 6 \times 10^{10}$), chosen arbitrarily for this test, determines the distribution n at equilibrium. We apply the same verification procedure as before. Parameters are given in Table S5 and Table S8.

As described in case 4 for STR processes, equilibrium solutions occur only for specific choices of aggregation and fragmentation kernels. However, even when an equilibrium solution exists, whether or not it can be observed depends on several time scales: 1. the time for the flow to reach the steady state; 2. the time when the observation is made; and 3. the reaction time required to reach the aggregation-fragmentation equilibrium if it exists. There are two requirements to observe the equilibrium solution at the outlet. First, the reaction time must be smaller than the time to achieve steady state. Otherwise only the transient behavior of the aggregation-fragmentation process can be

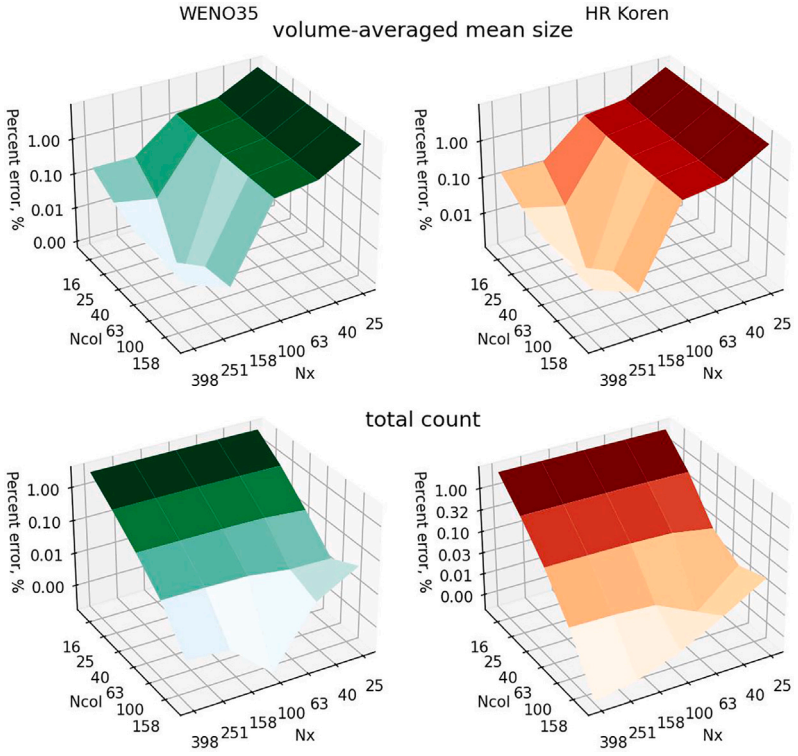

Fig. 12. Case 6: pure aggregation in a DPFR. Errors of the mean size and total count based on the outlet solution as a function of N_x-N_{col}.

observed. Second, the observation time must be larger than the time required to achieve steady state. Otherwise, only the transient behavior of the solute transport process can be observed. These requirements can be satisfied by carefully designing model parameters and observing the full solutions inside the DPFR. An example is shown in Fig. 7(c), where equilibrium was established near the end of the reactor.

As before, we observe similar Pareto fronts and performance for the WENO35 and HR Koren schemes, as depicted in Fig. 9(c). In either case, increasing N_x in the WFV and MCNP scheme led to an increased runtime at a rate of around 3.0 while increasing N_{col} only increased the runtime at a rate of 1.0. The EOC was found to be around 2.0 when increasing N_x or N_{col}. That these similar rates were observed for both the WENO35 and HR Koren schemes also explains Figure S17: to stay on the Pareto fronts, increasing N_x and N_{col} proportionally is efficient for both schemes.

The moments $M_{0,0}$ and $M_{3,0}$ in Figure S18 and Figure S20, the total particle count and mean size in Figure S19 behave similarly to the previous case where convergence and very small errors ($< 3.5\%$) even on coarse grids are observed.

5.9. Case 9: Nucleation, growth, growth rate dispersion and aggregation in a DPFR

In this test case, we combine the aggregation term considered in this work with the nucleation, growth, growth rate dispersion terms and the mass balance equation in our part I work. This test case is useful for continuous crystallization or precipitation processes (Raphael and Rohani, 1999; Alvarez and Myerson, 2010; Li et al., 2023; Ghosh et al., 2023). Here we consider a constant aggregation kernel combined with size-independent growth, growth rate dispersion and primary and secondary nucleation mechanisms. Model parameters can be found in Table S5 and Table S9. A full solution inside the DPFR is shown in Fig. 7(d). The testing procedure is the same as for case 6.

Regarding the Pareto fronts in Fig. 9(d), similar to the previous cases, the WENO35 and HR Koren scheme were equivalent in performance. We also found that increasing N_x increased the runtime at a rate of around 2.5 while a rate of 1.0 was observed when increasing N_{col} (Figure S21). The EOC was found to be around 3.0 when increasing either N_x or N_{col}. As shown in Fig. 13, we again observe that proportionally increasing N_x and N_{col} is most efficient to stay on the Pareto fronts.

Fig. 14(a) shows convergence behaviors of $M_{0,0}$ when increasing N_{col}. For other situations in Figs. 14(b), (c) and (d) where it is hard to quantify the errors visually, the normalized absolute errors are plotted in Figure S23. Compared to previous cases where there is only pure aggregation and/or fragmentation, errors in this case obviously increase: a maximum error of $\sim 14\%$ is observed for $M_{3,0}$ in Fig. 14(c) and (d). In contrast, a much smaller error of $< 1.3\%$ is observed in Fig. 14(b). This is not surprising as the growth and growth rate dispersion terms still preserve the zeroth order moment about x according to Section 3.5. Overall, these results align well with our previous findings such that these moments are no longer strictly conserved or preserved. Further, evaluating the errors of the total count and mean size of the outlet distribution in Figure S22, similar convergence behaviors are observed. This is expected as no moment is strictly preserved in this case.

6. Conclusions and outlook

This contribution is an extension to our part I work in which we solved the PBM in STR and DPFR formats while considering nucleation, growth, growth rate dispersion, axial convection and diffusion processes in the free and open-source process modeling package CADET. In this work, we further adapted the WFV and MCNP schemes to discretize the size-based Smoluchowski coagulation and fragmentation equations to account for particle aggregation and fragmentation processes. In addition to their formulation for an STR format, both equations were also formulated for a DPFR format that included axial convection and diffusion along the external coordinate.

All equations were implemented in CADET with analytical Jacobians derived and implemented to reduce the computation time. The implementations were further verified and benchmarked in nine case studies. The numerical approximations were in excellent agreement

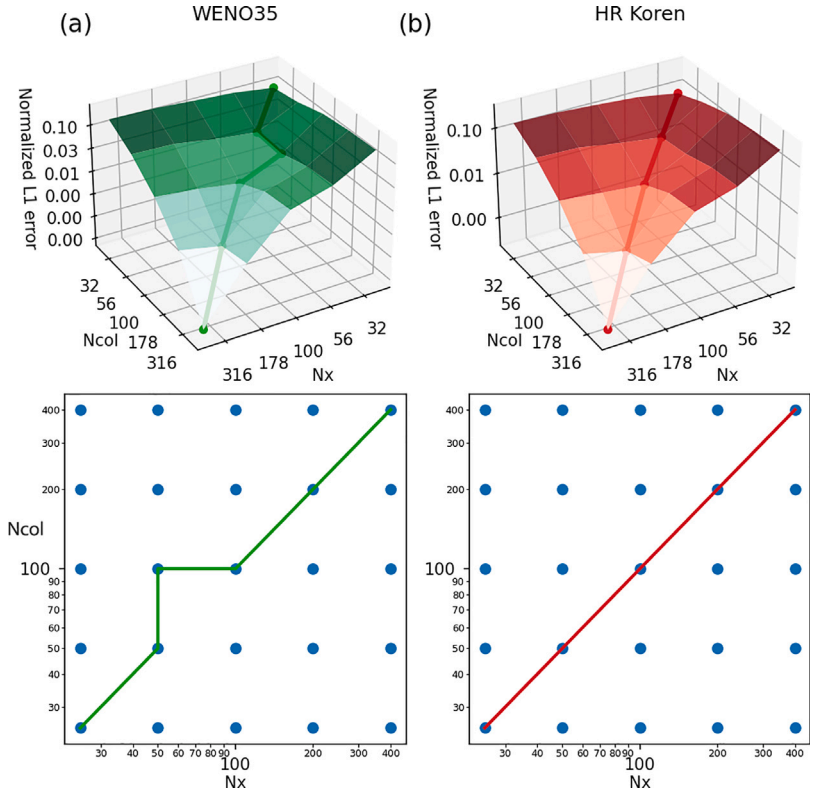

Fig. 13. Case 9: nucleation, growth, growth rate dispersion and aggregation in a DPFR. Top: Normalized L^1 error as a function of N_x and N_{col}. Solid lines are the Pareto fronts. Bottom: projections of the Pareto fronts to the N_x-N_{col} plane. (a): WENO35; (b): HR Koren.

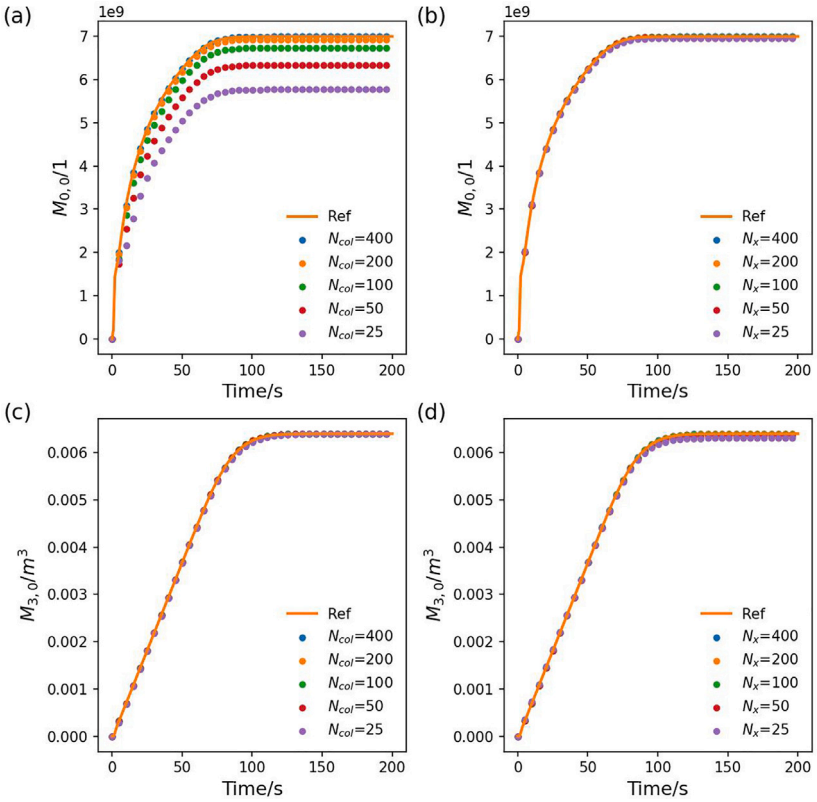

Fig. 14. Numerical and reference $M_{3,0}$ and $M_{0,0}$ for the entire reactor in case 9: (a): $M_{0,0}$ vs. N_{col}; (b): $M_{0,0}$ vs. N_x; (c): $M_{3,0}$ vs. N_{col}; (d): $M_{3,0}$ vs. N_x. Results were obtained using HR Koren scheme.

with analytical solutions when available. We observed second order convergence of the size-based WFV and MCNP schemes on logarithmic grids for the 1D cases. The second-order rate was attributed to the underlying second-order midpoint quadrature approximation. The zeroth and third order moments were accurately captured for all 1D cases. Although preservation of other order moments was not guaranteed theoretically, they were still approximated with high accuracy.

In the 2D cases, comprising particle processes occurring in the DPFR format, we compared both the WENO35 and HR Koren schemes as axial flux reconstruction methods. Both schemes gave similar results in all cases due to an overall second order convergence rate when combined with either the WFV or MCNP scheme. After a careful analysis of the normalized L^1 error and runtime, we found that increasing N_x and N_{col} proportionally reduced the error most efficiently for a given runtime.

Both the size-based WFV and MCNP schemes were proven to conserve and preserve total particle volume and particle count, respectively. However, these preservation properties depend on the boundary conditions when combined with other terms in the PBM. We mathematically proved and numerically verified that in 1D cases where growth and growth rate dispersion are considered, the total count is still preserved, but the total volume is not strictly conserved. Similarly, in the 2D cases, where axial convection and diffusion were considered, all moments were no longer strictly preserved. They are, however, accurate approximations except on very coarse grids. Convergent behaviors were also observed for their errors.

A future direction would be to provide a rigorous theoretical analysis of the convergence behaviors of the size-based WFV and MCNP schemes. Moreover, the high-order flux construction schemes could be modified to force the discretized 1D equations to conserve the third order moment (Kumar et al., 2013) when combined with growth terms, and a convergence analysis could be provided for the modified schemes. Another promising direction is the development of a higher order FEM to improve computational efficiency. A suitable FEM can be developed which preserves and conserves the zeroth and third order moments while retaining higher convergence order. Moreover, a stabilization mechanism can be considered to adequately resolve steep gradients when combined with nucleation and growth terms.

CRediT authorship contribution statement

Wendi Zhang: Writing – original draft, Visualization, Validation, Software, Methodology, Investigation, Formal analysis. **Todd Przybycien:** Writing – review & editing, Supervision, Resources, Project administration, Funding acquisition, Conceptualization. **Jan Michael Breuer:** Writing – review & editing, Software, Methodology. **Eric von Lieres:** Writing – review & editing, Supervision, Resources, Methodology.

Declaration of competing interest

The authors declare that they have no known competing financial interests or personal relationships that could have appeared to influence the work reported in this paper.

Data availability

Data will be made available on request.

Acknowledgments

Wendi Zhang was supported by the U.S. Food and Drug Administration, Contract No. 75F40121C00111. Any opinions, findings, conclusions, or recommendations expressed in this material are those of the authors and do not necessarily reflect the views of the financial sponsor.

This project has received funding from the Innovative Medicines Initiative 2 Joint Undertaking under grant agreement No 101007799 (Inno4Vac). This Joint Undertaking receives support from the European Union's Horizon 2020 research and innovation programme and EFPIA. This communication reflects the author's view and neither IMI nor the European Union, EFPIA, or any associated partners are responsible for any use that may be made of the information contained herein.

Appendix A. Supplementary data

Supplementary material related to this article can be found online at https://doi.org/10.1016/j.compchemeng.2024.108860.

References

Alvarez, A.J., Myerson, A.S., 2010. Continuous plug flow crystallization of pharmaceutical compounds. Cryst. Growth Des. 10 (5), 2219–2228. http://dx.doi.org/10.1021/cg901496s.

Bourgade, J.-P., Filbet, F., 2007. Convergence of a finite volume scheme for coagulation-fragmentation equations. Math. Comp. 77 (262), 851–883. http://dx.doi.org/10.1090/S0025-5718-07-02054-6, URL http://www.ams.org/journal-getitem?pii=S0025-5718-07-02054-6.

Eibeck, A., Wagner, W., 2000. Approximative solution of the coagulation–fragmentation equation by stochastic particle systems. Stoch. Anal. Appl. 18 (6), 921–948. http://dx.doi.org/10.1080/07362990008809704, URL http://www.tandfonline.com/doi/abs/10.1080/07362990008809704.

Eibeck, A., Wagner, W., 2001. Stochastic algorithms for studying coagulation dynamics and gelation phenomena. Monte Carlo Methods Appl. 7 (1–2), 157–165. http://dx.doi.org/10.1515/mcma.2001.7.1-2.157.

Filbet, F., Laurençot, P., 2004. Numerical simulation of the Smoluchowski coagulation equation. SIAM J. Sci. Comput. 25 (6), 2004–2028. http://dx.doi.org/10.1137/S1064827503429132, URL http://epubs.siam.org/doi/10.1137/S1064827503429132.

Forestier-Coste, L., Mancini, S., 2012. A finite volume preserving scheme on nonuniform meshes and for multidimensional coalescence. SIAM J. Sci. Comput. 34 (6), B840–B860. http://dx.doi.org/10.1137/110847998, URL http://epubs.siam.org/doi/10.1137/110847998.

Ghosh, S., Mergy, M., Minervini, M., Okpanum, J., Cramer, S.M., Bequette, B.W., Zydney, A.L., Przybycien, T.M., 2023. Smart manufacturing implementation of a continuous downstream precipitation and filtration process for antibody purification. Smart Sustain. Manuf. Syst. 7 (1), 129–147. http://dx.doi.org/10.1520/SSMS20230003.

Golovin, A., 1963. The solution of the coagulation equation for cloud droplets in a rising air current. Izv. Geophys. Ser 5 (4), 82–84.

Hailiang, L.I., Gropler, R., Warnecke, G., 2019. A high order positivity preserving DG method for coagulation-fragmentation equations. SIAM J. Sci. Comput. 41 (3), B448–B465. http://dx.doi.org/10.1137/17M1150360, arXiv:1710.00964.

Hindmarsh, A.C., Brown, P.N., Grant, K.E., Lee, S.L., Serban, R., Shumaker, D.E., Woodward, C.S., 2005. SUNDIALS. ACM Trans. Math. Softw. http://dx.doi.org/10.1145/1089014.1089020, URL https://dl.acm.org/doi/10.1145/1089014.1089020.

Hounslow, 1990. A Discretized Population Balance for Simultaneous Nucleation, Growth and Aggregation (Ph.D. thesis). University of Adelaide, URL https://hdl.handle.net/2440/19087.

Hounslow, M.J., Pearson, J.M.K., Instone, T., 2001. Tracer studies of high-shear granulation: II. Population balance modeling. AIChE J. 47 (9), 1984–1999. http://dx.doi.org/10.1002/aic.690470910, URL https://onlinelibrary.wiley.com/doi/10.1002/aic.690470910.

Hounslow, M.J., Ryall, R.L., Marshall, V.R., 1988. A discretized population balance for nucleation, growth, and aggregation. AIChE J. 34 (11), 1821–1832. http://dx.doi.org/10.1002/aic.690341108.

Kaur, G., Kumar, J., Heinrich, S., 2017. A weighted finite volume scheme for multivariate aggregation population balance equation. Comput. Chem. Eng. 101, 1–10. http://dx.doi.org/10.1016/j.compchemeng.2017.02.011.

Kumar, R., Kumar, J., 2013. Numerical simulation and convergence analysis of a finite volume scheme for solving general breakage population balance equations. Appl. Math. Comput. 219 (10), 5140–5151. http://dx.doi.org/10.1016/j.amc.2012.10.098.

Kumar, R., Kumar, J., Warnecke, G., 2013. Moment preserving finite volume schemes for solving population balance equations incorporating aggregation, breakage, growth and source terms. Math. Models Methods Appl. Sci. 23 (7).

Kumar, J., Peglow, M., Warnecke, G., Heinrich, S., Mörl, L., 2006. Improved accuracy and convergence of discretized population balance for aggregation: The cell average technique. Chem. Eng. Sci. 61 (10), 3327–3342. http://dx.doi.org/10.1016/j.ces.2005.12.014.

Kumar, S., Ramkrishna, D., 1996. On the solution of population balance equations by discretization—I. a fixed pivot technique. Chem. Eng. Sci. 51 (8), 1311–1332. http://dx.doi.org/10.1016/0009-2509(96)88489-2, URL https://linkinghub.elsevier.com/retrieve/pii/0009250996884892.

Lage, P.L., 2002. Comments on the "an analytical solution to the population balance equation with coalescence and breakage-the special case with constant number of particles" by D.P. Patil and J.R.G. Andrews [chemical engineering science 53(3) 599-601]. Chem. Eng. Sci. 57 (19), 4253–4254. http://dx.doi.org/10.1016/S0009-2509(02)00369-X.

LeVeque, R.J., 2002. Finite Volume Methods for Hyperbolic Problems. Cambridge University Press, http://dx.doi.org/10.1017/CBO9780511791253, URL https://www.cambridge.org/core/product/identifier/9780511791253/type/book.

Leweke, S., von Lieres, E., 2018. Chromatography analysis and design toolkit (CADET). Comput. Chem. Eng. 113, 274–294. http://dx.doi.org/10.1016/j.compchemeng.2018.02.025.

Li, Z., Chen, J., Martinez-Fonts, K., Rauscher, M., Rivera, S., Welsh, J., Kandula, S., 2023. Cationic polymer precipitation for enhanced impurity removal in downstream processing. Biotechnol. Bioeng. 120 (7), 1902–1913.

Lister, J.D., Smit, D.J., Hounslow, M.J., 1995. Adjustable discretized population balance for growth and aggregation. AIChE J. 41 (3), 591–603. http://dx.doi.org/10.1002/aic.690410317.

Mahoney, A.W., Ramkrishna, D., 2002. Efficient solution of population balance equations with discontinuities by finite elements. Chem. Eng. Sci. 57 (7), 1107–1119. http://dx.doi.org/10.1016/S0009-2509(01)00427-4.

Marchisio, D.L., Fox, R.O., 2005. Solution of population balance equations using the direct quadrature method of moments. J. Aerosol Sci. 36 (1), 43–73. http://dx.doi.org/10.1016/j.jaerosci.2004.07.009.

Müller, H., 1928. On the general theory of rapid coagulation. Kolloidchem. Beihefte 27 (6–12), 223–250. http://dx.doi.org/10.1007/BF02558510, URL http://link.springer.com/10.1007/BF02558510.

Patil, D.P., Andrews, J.R., 1998. An analytical solution to continuous population balance model describing floc coalescence and breakage - a special case. Chem. Eng. Sci. 53 (3), 599–601. http://dx.doi.org/10.1016/S0009-2509(97)00314-X.

Peterson, T.W., 1986. Similarity solutions for the population balance equation describing particle fragmentation. Aerosol Sci. Technol. 5 (1), 93–101. http://dx.doi.org/10.1080/02786828608959079.

Püttmann, A., Schnittert, S., Leweke, S., von Lieres, E., 2016. Utilizing algorithmic differentiation to efficiently compute chromatograms and parameter sensitivities. Chem. Eng. Sci. 139, 152–162. http://dx.doi.org/10.1016/j.ces.2015.08.050.

Qamar, S., Warnecke, G., 2007. Solving population balance equations for two-component aggregation by a finite volume scheme. Chem. Eng. Sci. 62 (3), 679–693. http://dx.doi.org/10.1016/j.ces.2006.10.001.

Randolph, A.D., Ranjan, R., 1977. Effect of a material-flow model in prediction of particle-size distributions in open- and closed-circuit mills. Int. J. Miner. Process. 4 (2), 99–110. http://dx.doi.org/10.1016/0301-7516(77)90019-9, URL https://linkinghub.elsevier.com/retrieve/pii/0301751677900199.

Raphael, M., Rohani, S., 1999. Sunflower protein precipitation in a tubular precipitator. Can. J. Chem. Eng. 77 (3), 540–554. http://dx.doi.org/10.1002/cjce.5450770315.

Saha, J., Bück, A., 2021. Improved accuracy and convergence analysis of finite volume methods for particle fragmentation models. Math. Methods Appl. Sci. 44 (2), 1913–1930. http://dx.doi.org/10.1002/mma.6890.

Saha, J., Kumar, J., Bück, A., Tsotsas, E., 2016. Finite volume approximations of breakage population balance equation. Chem. Eng. Res. Des. 110, 114–122. http://dx.doi.org/10.1016/j.cherd.2016.02.012.

Saito, O., 1958. Effects of high energy radiation on polymers II. end-linking and gel fraction. J. Phys. Soc. Japan 13 (12), 1451–1464.

Scott, W.T., 1968. Analytic studies of cloud droplet coalescence I. J. Atmos. Sci. 25 (1), 54–65. http://dx.doi.org/10.1175/1520-0469(1968)025<0054:ASOCDC>2.0.CO;2.

Singh, M., 2021. New finite volume approach for multidimensional Smoluchowski equation on nonuniform grids. Stud. Appl. Math. 147 (3), 955–977. http://dx.doi.org/10.1111/sapm.12415, URL https://onlinelibrary.wiley.com/doi/10.1111/sapm.12415.

Smit, D.J., Hounslow, M.J., Paterson, W.R., 1994. Aggregation and gelation-I. Analytical solutions for CST and batch operation. Chem. Eng. Sci. 49 (7), 1025–1035. http://dx.doi.org/10.1016/0009-2509(94)80009-X.

Smoluchowski, M.v., 1916. Three lectures on diffusion, brownian motion, and coagulation of colloidal particles. Zeitschrift fur Physik 17, 557–585.

Sorensen, C.M., Zhang, H.X., Taylor, T.W., 1987. Cluster-size evolution in a coagulation-fragmentation system. Phys. Rev. Lett. 59 (3), 363–366. http://dx.doi.org/10.1103/PhysRevLett.59.363, URL https://link.aps.org/doi/10.1103/PhysRevLett.59.363.

Vigil, R.D., 2009. On equilibrium solutions of aggregation-fragmentation problems. J. Colloid Interface Sci. 336 (2), 642–647. http://dx.doi.org/10.1016/j.jcis.2009.04.061.

Vigil, R., Ziff, R.M., 1989. On the stability of coagulation—fragmentation population balances. J. Colloid Interface Sci. 133 (1), 257–264. http://dx.doi.org/10.1016/0021-9797(89)90300-7, URL https://linkinghub.elsevier.com/retrieve/pii/0021979789903007.

von Lieres, E., Andersson, J., 2010. A fast and accurate solver for the general rate model of column liquid chromatography. Comput. Chem. Eng. 34 (8), 1180–1191. http://dx.doi.org/10.1016/j.compchemeng.2010.03.008, URL http://dx.doi.org/10.1016/j.compchemeng.2010.03.008.

Yuan, C., Laurent, F., Fox, R.O., 2012. An extended quadrature method of moments for population balance equations. J. Aerosol Sci. 51, 1–23. http://dx.doi.org/10.1016/j.jaerosci.2012.04.003.

Zhang, W., Przybycien, T., Schmölder, J., Leweke, S., von Lieres, E., 2024. Solving crystallization/precipitation population balance models in CADET, part I: Nucleation growth and growth rate dispersion in batch and continuous modes on nonuniform grids. Comput. Chem. Eng. 108612.